nature materials

Article

https://doi.org/10.1038/s41563-024-01856-6

A correlated ferromagnetic polar metal by design

Received: 28 June 2023

Accepted: 11 March 2024

Published online: 11 April 2024

Check for updates

Jianbing Zhang[1,16], Shengchun Shen[1,16], Danilo Puggioni[2,16], Meng Wang[1,16], Haozhi Sha[3,4,16], Xueli Xu[5], Yingjie Lyu[1], Huining Peng[1], Wandong Xing[3,4], Lauren N. Walters[2], Linhan Liu[3,4], Yujia Wang[1], De Hou[5], Chuanying Xi[5], Li Pi[5], Hiroaki Ishizuka[6], Yoshinori Kotani[7], Motoi Kimata[8], Hiroyuki Nojiri[8], Tetsuya Nakamura[9], Tian Liang[1,10,11], Di Yi[3], Tianxiang Nan[12], Jiadong Zang[13], Zhigao Sheng[5], Qing He[14], Shuyun Zhou[1,11], Naoto Nagaosa[10,15], Ce-Wen Nan[3], Yoshinori Tokura[10,15], Rong Yu[3,4] ✉, James M. Rondinelli[2] ✉ & Pu Yu[1,10,11] ✉

Polar metals have recently garnered increasing interest because of their promising functionalities. Here we report the experimental realization of an intrinsic coexisting ferromagnetism, polar distortion and metallicity in quasi-two-dimensional $Ca_3Co_3O_8$. This material crystallizes with alternating stacking of oxygen tetrahedral CoO_4 monolayers and octahedral CoO_6 bilayers. The ferromagnetic metallic state is confined within the quasi-two-dimensional CoO_6 layers, and the broken inversion symmetry arises simultaneously from the Co displacements. The breaking of both spatial-inversion and time-reversal symmetries, along with their strong coupling, gives rise to an intrinsic magnetochiral anisotropy with exotic magnetic field-free non-reciprocal electrical resistivity. An extraordinarily robust topological Hall effect persists over a broad temperature–magnetic field phase space, arising from dipole-induced Rashba spin–orbit coupling. Our work not only provides a rich platform to explore the coupling between polarity and magnetism in a metallic system, with extensive potential applications, but also defines a novel design strategy to access exotic correlated electronic states.

Traditionally, acentricity is seen as incompatible with metallicity due to the screening effect of free carriers on long-range dipole–dipole interactions. Nevertheless, Anderson and Blount proposed, based on a symmetry consideration, that metallic system can accommodate polar (ferroelectric-like) structural transitions, leading to the emergence of polar metals[1]. This idea has recently gained renewed attention due to the discovered novel electronic states and quantum functionalities in polar metals[2–15]. Numerous research efforts have been devoted to

[1]State Key Laboratory of Low Dimensional Quantum Physics and Department of Physics, Tsinghua University, Beijing, China. [2]Department of Materials Science and Engineering, Northwestern University, Evanston, IL, USA. [3]State Key Laboratory of New Ceramics and Fine Processing, School of Materials Science and Engineering, Tsinghua University, Beijing, China. [4]MOE Key Laboratory of Advanced Materials, Tsinghua University, Beijing, China. [5]High Magnetic Field Laboratory, HFIPS, Anhui, Chinese Academy of Sciences, Hefei, China. [6]Department of Physics, Tokyo Institute of Technology, Tokyo, Japan. [7]Center for Synchrotron Radiation Research, Japan Synchrotron Radiation Research Institute, Hyogo, Japan. [8]Institute of Materials Research, Tohoku University, Sendai, Japan. [9]International Center for Synchrotron Radiation Innovation Smart, Tohoku University, Sendai, Japan. [10]RIKEN Center for Emergent Matter Science (CEMS), Wako, Japan. [11]Frontier Science Center for Quantum Information, Beijing, China. [12]School of Integrated Circuits, Beijing National Research Center for Information Science and Technology, Tsinghua University, Beijing, China. [13]Department of Physics and Astronomy, University of New Hampshire, Durham, NH, USA. [14]Department of Physics, Durham University, Durham, UK. [15]Department of Applied Physics, University of Tokyo, Tokyo, Japan. [16]These authors contributed equally: Jianbing Zhang, Shengchun Shen, Danilo Puggioni, Meng Wang, Haozhi Sha. ✉e-mail: ryu@tsinghua.edu.cn; jrondinelli@northwestern.edu; yupu@tsinghua.edu.cn

https://doi.org/10.1038/s41563-024-01856-6

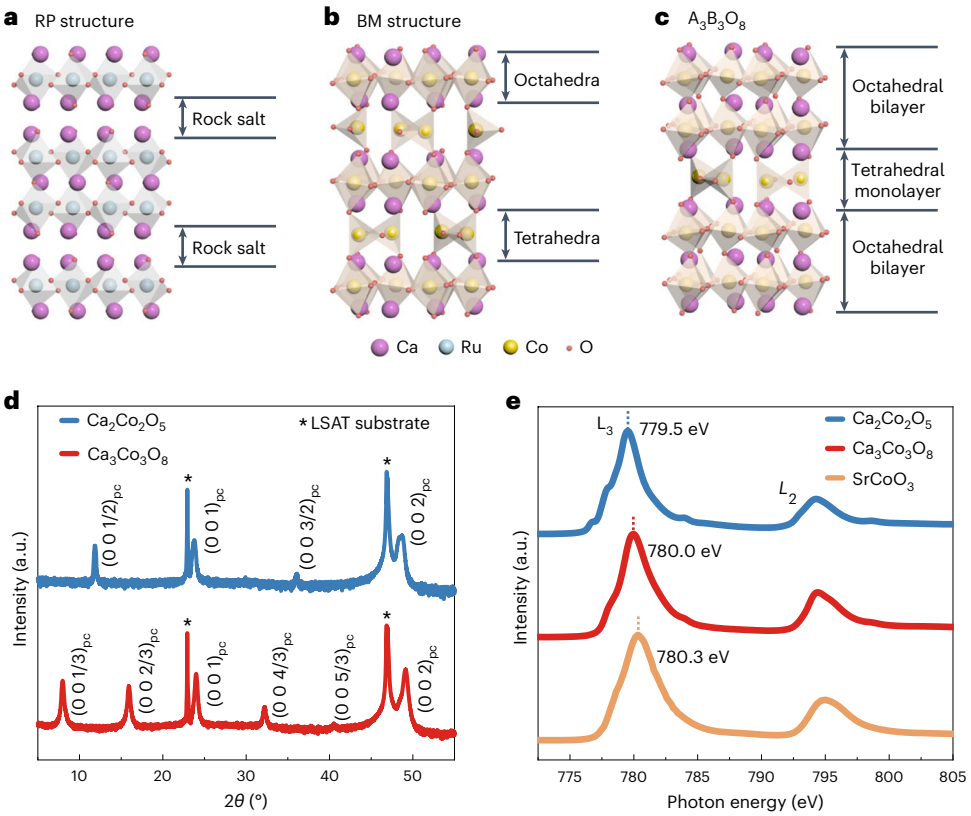

Fig. 1 | Experimental realization of $Ca_3Co_3O_8$. a–c, A direct comparison of the crystalline atomic structures of RP (**a**), brownmillerite (BM) (**b**) and the designed $Ca_3Co_3O_8$ (**c**), emphasizing the concept of structurally ordered oxygen vacancies. Purple, blue, yellow and red balls represent calcium, ruthenium, cobalt and oxygen atoms, respectively. **d**, High-resolution XRD 2θ–ω scans of $Ca_2Co_2O_5$ and $Ca_3Co_3O_8$ thin films, grown on LSAT (001) substrates. The pseudocubic notation (pc) was employed to denote the crystalline axes of both thin films. **e**, A direct comparison of X-ray absorption spectra at cobalt *L*-edges for $Ca_2Co_2O_5$, $Ca_3Co_3O_8$ and $SrCoO_3$. a.u., arbitrary unit.

exploring this concept, especially in complex oxides. The established strategies include introducing acentric ionic displacements whose electronic degrees of freedom are decoupled from the states at the Fermi level (weak coupling principle)[2–4], introducing metallicity into polar structures through chemical doping[5,6] or by fabricating artificial heterostructures combining acentricity and metallicity at interfaces[11,12]. Inspired by the promising magnetoelectric coupling observed in multiferroic materials[16], the introduction of magnetization into a polar metal opens up possibilities for attaining additional exotic phases that arise from the interplay between magnetic and polar orders[17–24]. This search has already motivated a series of experimental investigations[25–28] as well as theoretical proposals[29,30]. Nevertheless, the experimental realization of an intrinsic ferromagnetic (FM) polar metal with a robustly coupled ferromagnetism, polarity and metallicity remains challenging.

The challenge of realizing a FM polar metal lies in circumventing the conflicting requirements of polar displacements and metallicity, while at the same time incorporating suitable electron correlation to form a FM state. The weak coupling principle[4] is a widely used strategy to design polar metals, in which the polar displacements and metallicity are introduced through different sublattices, as successfully demonstrated in $LiOsO_3$ (ref. 2), $NdNiO_3$ (ref. 3) and anti-FM Ruddlesden–Popper (RP) $Ca_3Ru_2O_7$ (refs. 9,10) (Fig. 1a). However, in these cases, the polar distortion and metallicity are only weakly coupled due to their different origins. In the limited number of known FM polar metals such as magnetic ion (Mn)-doped GeTe ((Ge,Mn)Te) (ref. 26), Co-doped Fe_5GeTe_2 ($(Fe_{0.5}Co_{0.5})_5GeTe_2$) (refs. 27,28), etc., the atomic stacking is employed to geometrically break the inversion symmetry, in which the magnetization and polar distortion are only weakly coupled, while strong coupling constitutes an indispensable factor to achieve emerging electronic states[13,31–34]. Therefore, a new design strategy is highly demanded to integrate ferromagnetism into polar metals, and it explicitly requires that both polar atomic displacements and FM ordering originate from the same sublattice.

Rather than focusing on abundantly studied perovskites, we pursued our exploration from brownmillerite $A_2B_2O_5$ oxides in this study. These compounds have a perovskite-derivative structure, with alternating CoO_6 octahedral and CoO_4 tetrahedral Co–O layers due to ordered oxygen vacancies (Fig. 1b). In this structure, the breaking of inversion symmetry can be achieved via various pathways, such as tetrahedral-chain handedness[35], *A*-site cation ordering[36] and the incorporation of multiple phonon modes[37]. To integrate metallicity with similar oxygen vacancy ordered compounds, we constructed a crystalline structure with an alternative stacking of an oxygen octahedral bilayer and a tetrahedral monolayer, which can be formulated as $A_3B_3O_8$ (Fig. 1c). This structure reconciles the essential features of both double-layered RP and brownmillerite phases (Fig. 1a,b) and permits the tetrahedral monolayer to behave as the insulating rock-salt block in the RP compounds, providing an active quasi-two-dimensional (2D) electronic state in the octahedral bilayers. It is worth mentioning that similar $A_3B_3O_8$ compounds, such as $Ca_3Fe_2TiO_8$, $LaCa_2Fe_3O_8$ (ref. 38) and $La_3Co_3O_8$ (ref. 39) have been explored since the 1970s, while notably all these known compounds, also referred to as Grenier phases, exhibit insulating properties.

To harmonize the FM polar metallic state into the $A_3B_3O_8$ structure, cobalt was selected as the *B*-site element for its diverse oxidation states and coordination geometries (tetrahedral, octahedral and pyramidal), providing a promising route to obtain the designed crystal structure. Divalent calcium was chosen as the *A*-site element to achieve the mixed

https://doi.org/10.1038/s41563-024-01856-6

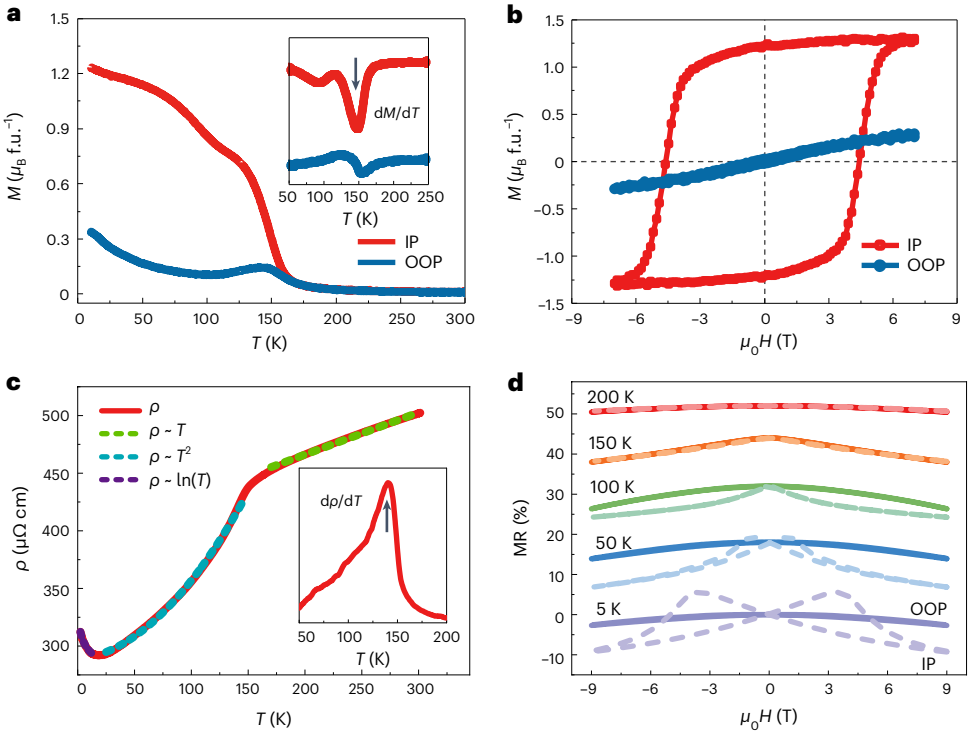

Fig. 2 | Magnetic and metallic properties of $Ca_3Co_3O_8$. a, Temperature-dependent magnetizations (M–T) measured along both the IP ($[100]_{pc}$) and OOP ($[001]_{pc}$) directions. IP and OOP are denoted by the thin-film geometry, while the $[001]_{pc}$ and $[100]_{pc}$ directions are assigned by the orientation of the LSAT substrate. The measurements were carried out at a magnetic field of 0.3 T after a magnetic field cooling with 7 T. **b**, IP and OOP magnetic hysteresis loops, measured at 5 K. **c**, The temperature-dependent electrical resistivity (ρ–T). **d**, IP (dashed lines) and OOP (solid lines) MR results measured at a series of representative temperatures. The MR curves above 5 K are shifted upwards for clarity. The insets in **a** and **c** show the derivative of the M–T and ρ–T curves, respectively, indicating the FM Curie temperature (T_C) around 150 K. f.u., formula unit. μ_B, Bohr magneton. μ_0, magnetic vacuum permeability.

valence of cobalt ions, which are conducive to both metallicity and ferromagnetism. To this end, we designed a hitherto-undiscovered compound, namely $Ca_3Co_3O_8$ (Fig. 1c).

To synthesize $Ca_3Co_3O_8$, we first started with its brownmillerite counterpart, $Ca_2Co_2O_5$ (ref. 40), and fabricated it into a high-quality thin-film form (Methods). The as-grown sample shows a periodic stacking of oxygen octahedra and tetrahedra along the film normal, as highlighted by the superlattice peaks in X-ray diffraction (XRD) data (Fig. 1d, blue curve). Then the $Ca_2Co_2O_5$ samples were post-annealed in ozone (Methods), after which a distinct structural transformation was triggered evidenced by the XRD data with tripled periodicity (Fig. 1d, red curve). The crystalline structure is of excellent quality, while the epitaxial strain is partially relaxed (Extended Data Fig. 1a–d). The film uniformity and atomic stacking sequence were further confirmed by subsequent high-resolution scanning transmission electron microscopy (STEM) measurements (Methods and Extended Data Fig. 1e–j). Furthermore, a buffered layer (about one pseudocubic unit cell) can be identified at the interface, which is essential to compensate the lattice mismatch. The mixed valence of Co ions with a Co^{4+}/Co^{3+} ratio of ~0.48 ± 0.04, was deduced from the soft X-ray absorption spectroscopy (XAS) measurements across cobalt L-edges[41] (Methods and Fig. 1e), which is consistent with the nominal valence state of $Ca_3Co_3O_8$. With these characterizations, we can ascertain that our de novo designed $Ca_3Co_3O_8$ has been successfully synthesized.

The temperature-dependent magnetization measurements (Fig. 2a) reveal a FM ground state with a Curie temperature of ~150 K. Interestingly, a large anisotropy was observed between magnetizations measured along the out-of-plane (OOP, along polyhedral stacking of $[001]_{pc}$) and in-plane (IP, $[100]_{pc}$) directions. This anisotropy is further supported by the M–H measurements (Fig. 2b and Extended Data Fig. 2a–f), where a rectangular-like hysteresis loop is observed along the IP direction, while the OOP measurements show a typical hard axis behaviour with unsaturated magnetization. The large magnetic anisotropy suggests a large spin–orbit coupling, for which element-specific X-ray magnetic circular dichroism (XMCD) measurements (Extended Data Fig. 2g) reveal a sizable orbital moment for Co ions with an m_{orb}/m_{spin} ratio of ~0.36.

$Ca_3Co_3O_8$ exhibits metallic behaviour in contrast to insulating $Ca_2Co_2O_5$, as shown in the temperature-dependent resistivity measurement of Fig. 2c. Excellent T^2 fitting below T_C describes a Fermi-liquid-like behaviour as compared with the linear T dependence above T_C. A slight upturn is observed at ~20 K, likely due to disorder-induced localization. It is worth noting that the resistivity is comparable with the Mott–Ioffe–Regel limit[42] (that is, ~400 μΩ cm), implying the presence of electron–electron interactions. The magnetoresistance (MR) (Fig. 2d) exhibits a set of well-defined butterfly-shaped loops (below T_C) along the IP direction, while no hysteresis was observed along the OOP direction for magnetic fields up to 9 T, confirming strong IP magnetic anisotropy and in agreement with the magnetization measurements (Fig. 2b). Extensive magnetization (Extended Data Fig. 3) and transport (Extended Data Fig. 4) measurements for films with the thickness of 20–120 nm, show a consistent FM Curie temperature (~150 K) and robust metallic state.

The macroscopic polar structure of $Ca_3Co_3O_8$ is revealed by the second harmonic generation (SHG) measurements (Methods). The optical SHG polar plot with p-polarized incident light, shown in Fig. 3a, indicates a unique polar axis along the film normal (OOP). However, an IP polar component cannot be fully excluded, since the small SHG response might be due to the small domain size arising from the lower IP symmetry of $Ca_3Co_3O_8$ compared with the $(LaAlO_3)_{0.3}$–$(SrAl_{0.5}Ta_{0.5}O_3)_{0.7}$ (LSAT) substrate. Figure 3b shows the temperature-dependent SHG measurements. The intensity of the (p, p) configuration remains finite

https://doi.org/10.1038/s41563-024-01856-6

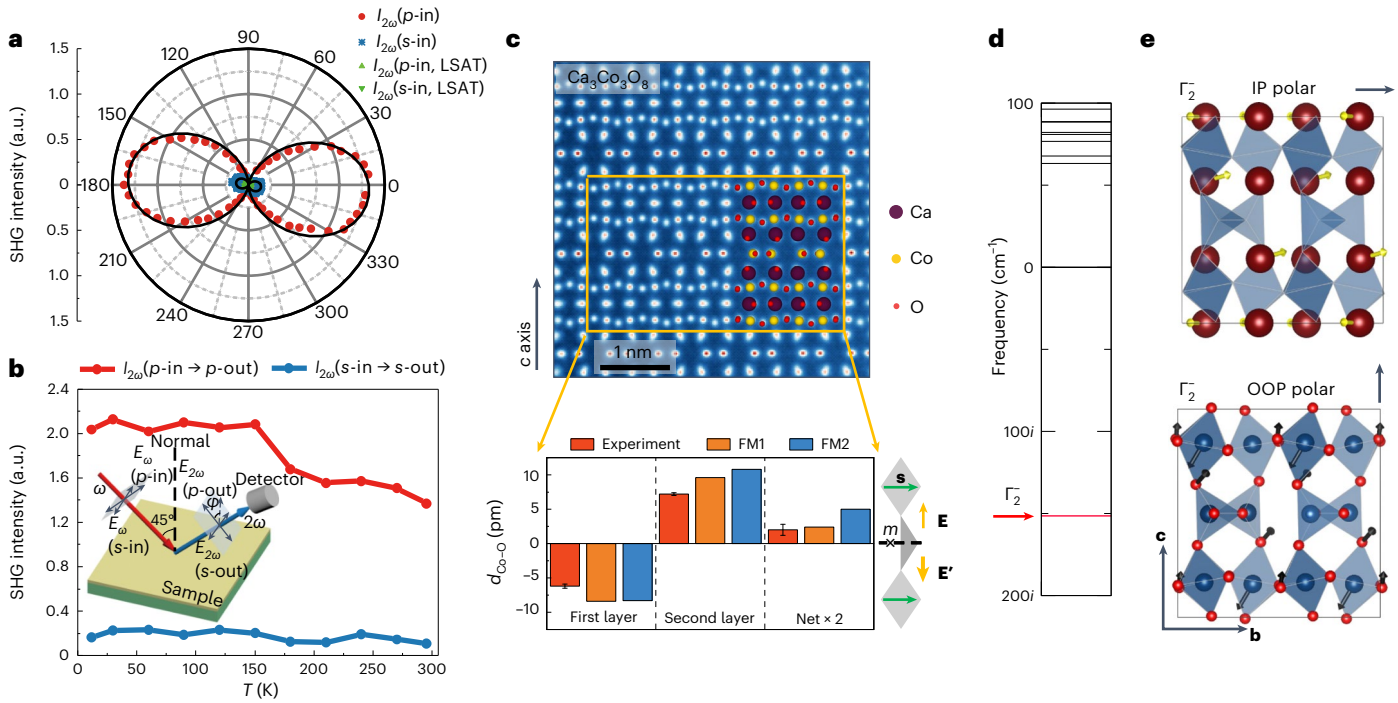

Fig. 3 | Evidence and mechanism of the polar state in $Ca_3Co_3O_8$. a, The polarization angle (φ) dependence of the SHG response. The data were measured at room temperature. The signals (green up and down triangles) from the LSAT substrate are also shown for comparison, which are too weak to be distinguished. **b**, The temperature-dependent SHG response. The polarization directions *p* and *s* are parallel and perpendicular to the incidence plane, respectively. Here, *p*-in, *s*-in, *p*-out and *s*-out indicate the polarization directions (*p*, *s*) of the incident (in) and emergent (out) lights, respectively, as labelled in the inset. ω, the fundamental frequency. E_ω and $E_{2\omega}$, the electric field intensities at the fundamental frequency ω and the doubled frequency 2ω, respectively. **c**, A ptychographic phase image measured at room temperature. The bar charts show averaged experimental relative shifts (d_{Co-O}) along the *c* axis between Co atom and neighbour equatorial O atoms at two different octahedral layers (at room temperature), and the calculated results for different magnetic states. The net relative shift is a summation between these two layers, which is notably larger than the standard error. The illustration indicates the coupling between the build-in OOP electric field **E** and IP spins **S**, resulting in a Rashba spin–orbit coupling. The **E** and **E′** with opposite directions are not equal in magnitude as a result of the broken mirror (*m*) symmetry. Experimental data are presented as mean values ± standard error of the mean (error bar) from the relative shifts of $n = 20$ Co atoms. The purple, yellow and red circles represent the calcium, cobalt and oxygen atoms, respectively. **d**, The calculated phonon frequencies at Γ point for the FM (FM1) centrosymmetric $P2_1/c$ phase. **e**, A schematic illustration of atomic displacements in the Γ_2^- polar mode for the FM2 phase. In the FM2 state, all spins within octahedra are coupled ferromagnetically, while the spins in tetrahedra are coupled antiferromagnetically within the layer. Only the main atomic contributions are shown for clarity.

up to room temperature with a drop near T_C, indicating a coupling between magnetism and the polar state[43]. This result implies that the origin of the polar state is not determined by the long-range magnetic order, but rather enhanced by its onset. To explore the polar state microscopically, electron ptychographic measurements (Extended Data Fig. 5a–c) at deep-subangstrom resolution and subpicometre accuracy were performed (Methods). In contrast to the negligible relative Co displacements in $Ca_2Co_2O_5$ (Extended Data Fig. 5d,f), large Co displacements were observed in $Ca_3Co_3O_8$, in which the average relative shifts d_{Co-O} of two octahedral layers within a single unit cell are opposite and unequal, resulting in a net shift of ~1.0 pm along the OOP direction (Fig. 3c and Extended Data Fig. 5e,g).

To understand why Co displacement occurs in $Ca_3Co_3O_8$, we performed first-principles density functional theory plus Hubbard (DFT + *U*) calculations (Methods). We started the analysis by performing full relaxations of two centrosymmetric structures with *Pbam* and $P2_1/c$ symmetries (Extended Data Figs. 6a,b), respectively, both with all Co ions ferromagnetically aligned (FM1) (Extended Data Fig. 7a). The centrosymmetric $P2_1/c$ phase was found to be 52 meV f.u.$^{-1}$ lower in energy compared with the *Pbam* phase, making it a good candidate for the reference state. The phonon calculations (Fig. 3d) reveal an unstable phonon mode (Γ_2^- symmetry) with a frequency of 151*i* cm^{-1} (*i* defines an imaginary number). By freezing such unstable phonon mode, a polar *Pc* phase (Extended Data Fig. 6c) was obtained with polar displacements along both the *c* axis (OOP, as experimentally identified) and the *b* axis (IP) (Extended Data Fig. 6d,e). Group-theoretical analysis reveals that the main contribution to the OOP and IP polar distortions (Γ_2^- mode) originate from the Co cations at the octahedral (O_h) sites and O ions. Importantly this relaxed *Pc* structure with a FM1 spin configuration, sufficing as a minimal model of the paramagnetic state, is only 1 meV f.u.$^{-1}$ lower in energy than the centrosymmetric phase $P2_1/c$.

Following the anti-FM alignment of local magnetic moments within the tetrahedra layers as revealed by the XMCD measurements (Extended Data Fig. 2g), we constructed a spin configuration with only the spins at octahedral layers ferromagnetically coupled (FM2 as shown in Extended Data Fig. 7b) and performed a full structural relaxation for the *Pc* phase. Consequently, we found a further 90 meV f.u.$^{-1}$ energy gain for the polar structure with respect to the FM1 spin configuration. The FM2 *Pc* structure also exhibits larger polar displacement (Fig. 3c). Specifically, the absolute amplitude of the Γ_2^- mode is 0.05 Å and 0.11 Å in the FM1 and FM2 configurations, respectively, indicating a large coupling between magnetism and polar displacements even in the presence of free carriers. Although the Γ_2^- mode in both spin configurations is qualitatively the same (Fig. 3e and Extended Data Fig. 6d,e), a major difference exists. The polar Co displacements at the tetrahedral sites (T_d) can be neglected in the FM1 structure, however, they are enhanced in the FM2 phase, compensating for some of the Co displacements in the O_h sites. Consequently, in the FM2 phase, the main contribution to the OOP polar distortion is due to half of the Co cations at the O_h sites, whereas the Ca cations mainly contribute to the IP polar distortion. We note that the assumption of the FM2 spin configuration in the centrosymmetric $P2_1/c$ phase results in the *Pc′* magnetic space

https://doi.org/10.1038/s41563-024-01856-6

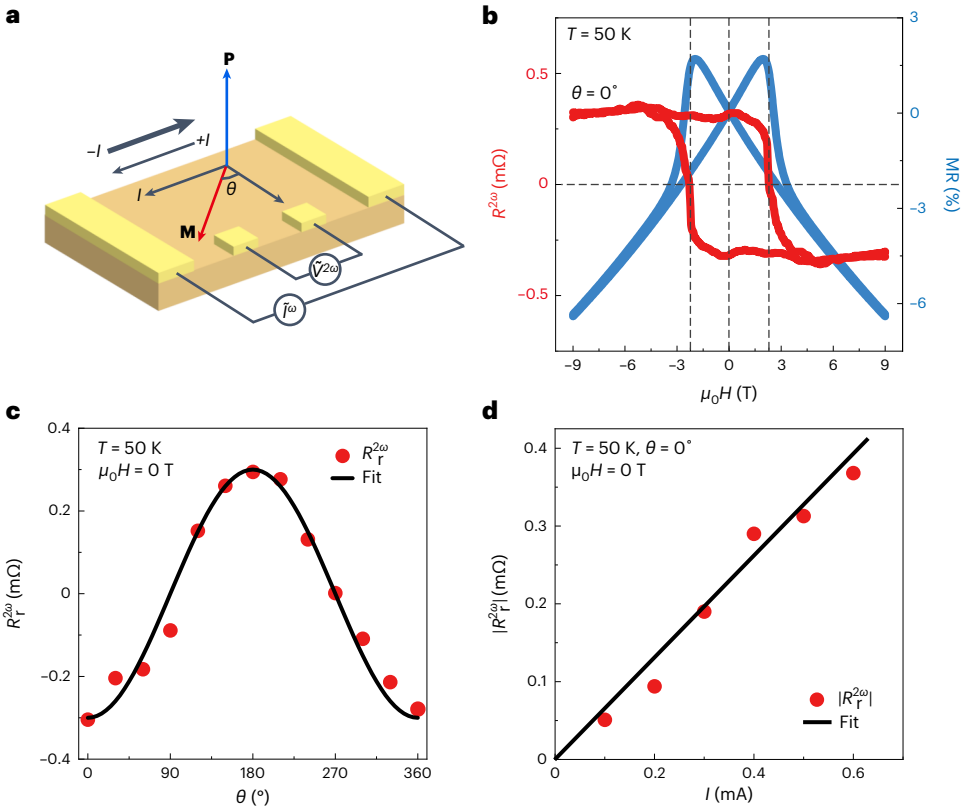

Fig. 4 | Non-reciprocal electrical transport in $Ca_3Co_3O_8$. a, A schematic illustration of the experimental configuration. **P** and **M** denote the vectors of polarization and magnetization, respectively, and θ is the angle between the magnetization and the normal of electric current (I) as labelled. The current (I) is along the $[100]_{pc}$ direction of the substrate. **b**, The non-reciprocal resistance ($R^{2\omega}$) and IP MR as a function of the magnetic field. The magnetic field was applied along the $[010]_{pc}$ direction ($\theta = 0°$), and the excitation current was set as 0.5 mA. The peaks of MR mark the positions of the coercive field with the magnetization reversal. **c**, The angular dependence of the remanent $R^{2\omega}$. The remanent $R_r^{2\omega}$ data denote the $R^{2\omega}$ at zero magnetic field, with the magnetic field sweeping from positive to zero. The curve is fitted by a cosine function. **d**, The remanent $R_r^{2\omega}$ as a function of I, showing a linear dependence. The measurements were carried out at 50 K.

group, and accordingly the $P2_1/c$ structure relaxes spontaneously to the Pc symmetry.

Consistent with the experimental results (Extended Data Fig. 2h), the calculations reveal the hybridization between the O 2p states and the Co 3d states in the valence band. Specifically, the atomic projected density of states (DOS) results (Extended Data Figs. 7b,c) and the local magnetic moments suggest a Co^{3+} $\underline{L}$ state (d^6 intermediate spin) for the O_{h1} magnetic site and a Co^{2+} $\underline{L}$ state (d^7 high spin) for both the O_{h2} and T_d site, where $\underline{L}$ indicates a ligand hole that originates from the strong 3d–2p hybridization. We note that, theoretically, the metallicity remains robust even for the G-type anti-FM order in this material[44], albeit with higher total energy by ~1.6 eV as compared with that of FM2 (Extended Data Figs. 7d,e).

Importantly, the electronic configurations of the Co cations circumvent the difficulty faced by electron doping of conventional ferroelectrics (for example, $BaTiO_3$)[5,6], in which the electron-doped Ti ion (d^1) prohibits the pseudo-Jahn–Teller effect (PJTE) activity[45,46]. In stark contrast, d^6 intermediate- and d^7 high-spin configurations observed here are all PJTE active[45] while simultaneously permitting a large carrier concentration. To support this concept, we introduced 0.2 electrons per Co atom in the Pc phase and performed atomic relaxations, and the polar distortion is reduced by only 28%. This situation is dramatically different from that of $BaTiO_3$, where acentricity is lost upon an electron doping of 0.1 electrons per Ti atom[46]. The inherent polar distortions in $Ca_3Co_3O_8$, resulting from the spontaneous displacements of the Co ions within the octahedral bilayers, contrast markedly with the geometrically embedded polar state as observed in the telluride compounds[26–28].

We note that competing orders in correlated materials can lead to exotic electronic and magnetic phenomena, including magnetochiral anisotropy[20] when the polarization (or electric field), magnetization (or magnetic field) and current direction are orthogonal to each other. Specifically, the coupling of the OOP polarization (P) and IP magnetization (M) in $Ca_3Co_3O_8$ gives rise to a current-directional-dependent resistance difference (non-reciprocal resistance), $R(I) - R(-I) \propto \boldsymbol{I} \cdot (\boldsymbol{P} \times \boldsymbol{M}) \propto IM\cos\theta$ (ref. 20), where θ is the angle between M and the normal direction of I (Fig. 4a). This non-reciprocal resistance can be clearly identified by measuring the second harmonic signal[19–22] ($R^{2\omega} \propto R_0 M I_0 \cos\theta$) of the resistivity upon applying an a.c. excitation current (Methods). Figure 4b shows the measured non-reciprocal resistance ($R^{2\omega}$) as a function of the magnetic field applied along $[010]_{pc}$, in which the $R^{2\omega}$ displays a clear hysteresis, which systematically changes sign when the magnetization is reversed. We emphasize that the $R^{2\omega}$ in $Ca_3Co_3O_8$ shows a well-defined remanent component, in sharp contrast to that observed in nonmagnetic polar metal systems[18–20,22]. Additionally, the remanent component, $R_r^{2\omega}$, shows a cosine dependence of θ in accordance with the above discussions (Fig. 4c). Moreover, the non-reciprocal resistance is a nonlinear effect[20], and thus the remanent $R_r^{2\omega}$ is proportional to the magnitude of the electric current (I) (Fig. 4d). These measurements directly demonstrate the coupling between the polarization and magnetization, which leads to a deformed band structure with lifted Kramer's degeneracy[20]. The temperature-dependent measurements (Supplementary Fig. 1 and Supplementary Note 1) reveal that the non-reciprocal resistance persists up to the Curie temperature, while the amplitude decreases rapidly

https://doi.org/10.1038/s41563-024-01856-6

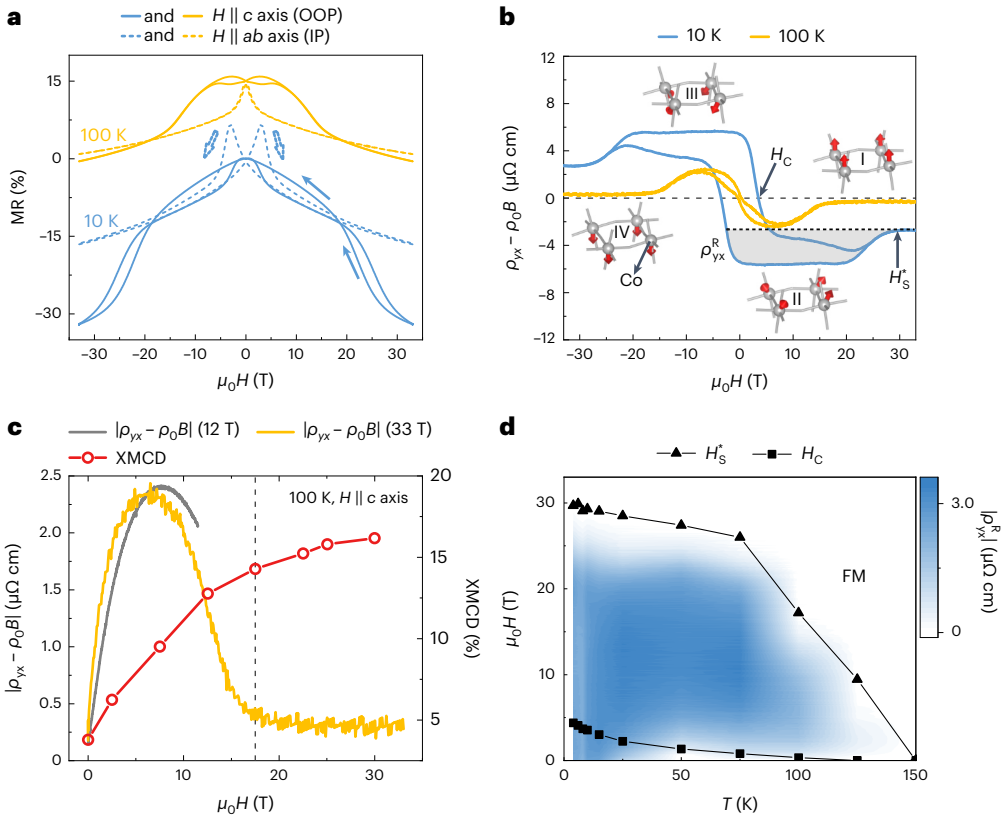

Fig. 5 | Robust THE in $Ca_3Co_3O_8$. a,**b**, The MR (**a**) and Hall resistivity (**b**) of $Ca_3Co_3O_8$ under the application of high magnetic field up to 33 T. The measurements were carried out at both 10 and 100 K, with the magnetic field applied along both *c* axis (OOP, solid lines) and *ab* plane (IP, dashed lines). Note that the total Hall resistivity is given by $\rho_{yx} = \rho_0 B + R_s M + \rho^T_{yx}$, where the first term is the ordinary Hall effect, the second term is the AHE and the last term is the THE resulting from skyrmion or other non-coplanar textures[24]. Here, the ordinary Hall contribution was removed by fitting the linear background at the high field region. To quantify the THE, we denote ρ^R_{yx} as the residual Hall component by subtracting the Hall signal with the ordinary Hall components as well as the saturated (at high field) anomalous Hall component, which is outlined by the grey region in **b**. The insets show schematic evolution of spin configurations within octahedral layers. **c**, The magnetic field dependence of the THE and magnetization at 100 K. The grey and orange curves represent Hall resistivity with ordinary Hall contribution removed under magnetic field up to 12 and 33 T, respectively. The red curve was obtained from a XMCD study. **d**, A temperature–magnetic field diagram of the THE. FM represents the collinear FM state. H_c (squares) represents the coercive field, and H_s^* (triangles) represents the saturated point for FM.

with increasing temperature with a sign change at about 75 K, which is attributed to the evolution of Berry curvature[20] at different temperatures.

Furthermore, we demonstrate that the polarization state can be manipulated through a tip-pressure-induced strain gradient through flexoelectric coupling[47], as evidenced by the systematic evolution of the remanent non-reciprocal resistance with loading pressure (Supplementary Fig. 2 and Supplementary Note 2). Due to the fact that the polarity is driven by the PJTE in the current system, we expect that its polar state can be further manipulated through optical means[48,49] as demonstrated recently in quantum paraelectric strontium titanite systems. Furthermore, with the coupling between the polarity and magnetism, it would be promising to realize the optical control of magnetism in the current system, which is of fundamental importance to obtain high-speed spintronic devices.

Intriguingly, the polar distortion can also lead to exotic spin textures in $Ca_3Co_3O_8$, due to a strong Rashba spin–orbit coupling as conceptually illustrated in Fig. 3c. The Rashba field results in a Dzyaloshinskii–Moriya (DM) interaction with the DM vector oriented along the IP direction (Supplementary Note 3). We note that similar DM interactions underpin the skyrmions observed in many magnetic heterostructures[23,24], which might lead to the emergence of non-collinear/non-coplanar spin configurations in $Ca_3Co_3O_8$ as well. Figure 5a shows a representative MR result with high magnetic fields (up to 33 T) applied along both the IP and OOP directions. While a conventional butterfly-like curve was observed for IP magnetic fields, two prominent crossing points were identified for the OOP case, which can be attributed to the switching between different magnetic states. This magnetic switching couples with the itinerant metallic state, producing a fascinating Hall effect. The Hall data with the ordinary Hall contribution removed (Fig. 5b,c) exhibit a non-monotonic hump feature superimposed on anomalous Hall effect (AHE) below the saturated magnetic field (for example, $H_s^* \approx 29$ T at 10 K), which is a hallmark of the topological Hall effect (THE; Supplementary Note 4), although at the same region the magnetization increases monotonically with the magnetic fields (XMCD in Fig. 5c and Extended Data Fig. 8). This distinction suggests the formation of non-collinear/non-coplanar spin configurations[24], as sketched in the inset of Fig. 5b. Under a large magnetic field ($|H| > H_s^*$) along the OOP, the magnetic moments are fully polarized into a FM state (Fig. 5b, inset, I and IV), and the Hall signal is saturated predominately towards the AHE component. When the field strength is reduced, the DM interaction leads to canted spins forming possibly non-collinear/non-coplanar configurations (Fig. 5b, inset, II and III), where a hump feature, attributed to the THE, can be clearly identified from the Hall signal. Strikingly, in this study the THE persists throughout a wide temperature and large magnetic field range (Fig. 5d and Extended Data Fig. 9a), which is starkly different from the conventional skyrmion systems (for example, $(Fe_{0.5}Co_{0.5})_5GeTe_2$; Supplementary

Table 1 in Supplementary Note 5), where the THE is found only in narrow temperature–magnetic field regions[23,24]. Furthermore, under the application of tilted magnetic field, the THE (hump feature) is systematically suppressed (Extended Data Figs. 9c,d), which can rule out the possibility of two channel AHE (Supplementary Fig. 3 in Supplementary Note 4) and is consistent with the skyrmion instability scenario[23,24]. The subsequent magnetic force microscopy (MFM; Methods) imaging explicitly shows a close correlation between the THE signal (hump feature) and Néel-type magnetic domain density (Extended Data Fig. 10), which indicates the THE arises from the emergent magnetic field in a non-coplanar spin texture characterized by scalar spin chirality (Supplementary Note 4) due to Rashba interactions[50].

Magnetic skyrmion and related spin textures have emerged as a promising candidate for data storage, which however face the challenges of thermal and magnetic-field instability as they typically occur in a narrow temperature–magnetic field region[23,24]. Therefore, the extremely robust THE and spin textures observed in the current system would be beneficial for the application of nonvolatile data storage. Furthermore, the coupling between the polarity and magnetism offer the possibility to obtained the control of magnetic states through electrical and optical pathways for highly energy-efficient and high-speed devices.

To summarize, we designed and realized a correlated FM polar metal, $Ca_3Co_3O_8$, which exhibits a magnetic field-free magnetochiral anisotropy and an extraordinarily robust THE. We envision that this material and its derivatives will serve as a model family to probe the rich spectrum of emergent states with the coupled polarity, magnetism and metallicity, leading to intriguing functionalities for electrical and spintronic devices. The oxygen vacancy ordering concept opens a new frontier to design and unify disparate magnetic and electronic properties in correlated functional oxides.

Online content

Any methods, additional references, Nature Portfolio reporting summaries, source data, extended data, supplementary information, acknowledgements, peer review information; details of author contributions and competing interests; and statements of data and code availability are available at https://doi.org/10.1038/s41563-024-01856-6.

References

1. Anderson, P. W. & Blount, E. I. Symmetry considerations on martensitic transformations: 'ferroelectric' metals? *Phys. Rev. Lett.* **14**, 217–219 (1965).
2. Shi, Y. G. et al. A ferroelectric-like structural transition in a metal. *Nat. Mater.* **12**, 1024–1027 (2013).
3. Kim, T. H. et al. Polar metals by geometric design. *Nature* **533**, 68–72 (2016).
4. Puggioni, D. & Rondinelli, J. M. Designing a robustly metallic noncenstrosymmetric ruthenate oxide with large thermopower anisotropy. *Nat. Commun.* **5**, 3432 (2014).
5. Kolodiazhnyi, T., Tachibana, M., Kawaji, H., Hwang, J. & Takayama-Muromachi, E. Persistence of ferroelectricity in $BaTiO_3$ through the insulator–metal transition. *Phys. Rev. Lett.* **104**, 147602 (2010).
6. Fujioka, J. et al. Ferroelectric-like metallic state in electron doped $BaTiO_3$. *Sci. Rep.* **5**, 13207 (2015).
7. Filippetti, A., Fiorentini, V., Ricci, F., Delugas, P. & Iniguez, J. Prediction of a native ferroelectric metal. *Nat. Commun.* **7**, 11211 (2016).
8. Benedek, N. A. & Birol, T. 'Ferroelectric' metals reexamined: fundamental mechanisms and design considerations for new materials. *J. Mater. Chem. C* **4**, 4000–4015 (2016).
9. Lei, S. M. et al. Observation of quasi-two-dimensional polar domains and ferroelastic switching in a metal, $Ca_3Ru_2O_7$. *Nano Lett.* **18**, 3088–3095 (2018).
10. Markovic, I. et al. Electronically driven spin-reorientation transition of the correlated polar metal $Ca_3Ru_2O_7$. *Proc. Natl Acad. Sci. USA* **117**, 15524–15529 (2020).
11. Hwang, H. Y. et al. Emergent phenomena at oxide interfaces. *Nat. Mater.* **11**, 103–113 (2012).
12. Lesne, E. et al. Highly efficient and tunable spin-to-charge conversion through Rashba coupling at oxide interfaces. *Nat. Mater.* **15**, 1261–1266 (2016).
13. Fei, Z. Y. et al. Ferroelectric switching of a two-dimensional metal. *Nature* **560**, 336–339 (2018).
14. Edelstein, V. M. Inverse Faraday effect in conducting crystals caused by a broken mirror symmetry. *Phys. Rev. Lett.* **80**, 5766–5769 (1998).
15. Sakai, H. et al. Critical enhancement of thermopower in a chemically tuned polar semimetal $MoTe_2$. *Sci. Adv.* **2**, e1601378 (2016).
16. Spaldin, N. A. & Ramesh, R. Advances in magnetoelectric multiferroics. *Nat. Mater.* **18**, 203–212 (2019).
17. Rikken, G. & Wyder, P. Magnetoelectric anisotropy in diffusive transport. *Phys. Rev. Lett.* **94**, 016601 (2005).
18. Yasuda, K. et al. Large unidirectional magnetoresistance in a magnetic topological insulator. *Phys. Rev. Lett.* **117**, 127202 (2016).
19. Ideue, T. et al. Bulk rectification effect in a polar semiconductor. *Nat. Phys.* **13**, 578–583 (2017).
20. Tokura, Y. & Nagaosa, N. Nonreciprocal responses from non-centrosymmetric quantum materials. *Nat. Commun.* **9**, 3740 (2018).
21. Yasuda, K. et al. Large non-reciprocal charge transport mediated by quantum anomalous Hall edge states. *Nat. Nanotechnol.* **15**, 831–835 (2020).
22. Lee, J. H. et al. Nonreciprocal transport in a Rashba ferromagnet, delafossite $PdCoO_2$. *Nano Lett.* **21**, 8687–8692 (2021).
23. Fert, A., Reyren, N. & Cros, V. Magnetic skyrmions: advances in physics and potential applications. *Nat. Rev. Mater.* **2**, 17031 (2017).
24. Tokura, Y. & Kanazawa, N. Magnetic skyrmion materials. *Chem. Rev.* **121**, 2857–2897 (2021).
25. Stornaiuolo, D. et al. Tunable spin polarization and superconductivity in engineered oxide interfaces. *Nat. Mater.* **15**, 278–283 (2016).
26. Yoshimi, R. et al. Current-driven magnetization switching in ferromagnetic bulk Rashba semiconductor (Ge,Mn)Te. *Sci. Adv.* **4**, eaat9989 (2018).
27. Zhang, H. et al. Room temperature skyrmion lattice in a layered magnet $(Fe_{0.5}Co_{0.5})_5GeTe_2$. *Sci. Adv.* **8**, eabm7103 (2022).
28. Zhang, H. et al. A room temperature polar magnetic metal. *Phys. Rev. Mater.* **6**, 044403 (2022).
29. Urru, A., Ricci, F., Filippetti, A., Iniguez, J. & Fiorentini, V. A three-order-parameter bistable magnetoelectric multiferroic metal. *Nat. Commun.* **11**, 4922 (2020).
30. Duan, X., Huang, J. W., Xu, B. & Liu, S. A two-dimensional multiferroic metal with voltage-tunable magnetization and metallicity. *Mater. Horiz.* **8**, 2316–2324 (2021).
31. Xu, S. Y. et al. Discovery of a Weyl fermion semimetal and topological Fermi arcs. *Science* **349**, 613–617 (2015).
32. Soluyanov, A. A. et al. Type-II Weyl semimetals. *Nature* **527**, 495–498 (2015).
33. Lu, J. M. et al. Evidence for two-dimensional Ising superconductivity in gated MoS_2. *Science* **350**, 1353–1357 (2015).
34. Deng, K. et al. Experimental observation of topological Fermi arcs in type-II Weyl semimetal $MoTe_2$. *Nat. Phys.* **12**, 1105–1110 (2016).
35. Parsons, T. G., D'Hondt, H., Hadermann, J. & Hayward, M. A. Synthesis and structural characterization of $La_{1-x}A_xMnO_{2.5}$ (A = Ba, Sr, Ca) phases: mapping the variants of the brownmillerite structure. *Chem. Mater.* **21**, 5527–5538 (2009).

36. Young, J. et al. Polar oxides without inversion symmetry through vacancy and chemical order. *J. Am. Chem. Soc.* **139**, 2833–2841 (2017).
37. Tian, H. et al. Novel type of ferroelectricity in brownmillerite structures: a first-principles study. *Phys. Rev. Mater.* **2**, 084402 (2018).
38. Grenier, J.-C., Darriet, J., Pouchard, M. & Hagenmuller, P. Mise en evidence d'une nouvelle famille de phases de type perovskite lacunaire ordonnee de formule $A_3M_3O_8$ ($AMO_{2.67}$). *Mater. Res. Bull.* **11**, 1219–1225 (1976).
39. Hansteen, O. H., Fjellvåg, H. & Hauback, B. C. Crystal structure, thermal and magnetic properties of $La_3Co_3O_8$. Phase relations for $LaCoO_{3-\delta}$ ($0.00 \leq \delta \leq 0.50$) at 673 K. *J. Mater. Chem.* **8**, 2081–2088 (1998).
40. Zhang, J. et al. Brownmillerite $Ca_2Co_2O_5$: Synthesis, stability, and re-entrant single crystal to single crystal structural transitions. *Chem. Mater.* **26**, 7172–7182 (2014).
41. Lu, N. et al. Electric-field control of tri-state phase transformation with a selective dual-ion switch. *Nature* **546**, 124–128 (2017).
42. Gunnarsson, O., Calandra, M. & Han, J. E. Colloquium: saturation of electrical resistivity. *Rev. Mod. Phys.* **75**, 1085–1099 (2003).
43. Lei, S. et al. Comprehensive magnetic phase diagrams of the polar metal $Ca_3(Ru_{0.95}Fe_{0.05})_2O_7$. *Phys. Rev. B* **99**, 224411 (2019).
44. Hudspeth, J. M., Goossens, D. J., Studer, A. J., Withers, R. L. & Norén, L. The crystal and magnetic structures of $LaCa_2Fe_3O_8$ and $NdCa_2Fe_3O_8$. *J. Phys. Condens. Matter* **21**, 124206 (2009).
45. Bersuker, I. B. Pseudo-Jahn–Teller effect-a two-state paradigm in formation, deformation, and transformation of molecular systems and solids. *Chem. Rev.* **113**, 1351–1390 (2013).
46. Hickox-Young, D., Puggioni, D. & Rondinelli, J. M. Persistent polar distortions from covalent interactions in doped $BaTiO_3$. *Phys. Rev. B* **102**, 014108 (2020).
47. Zabalo, A. & Stengel, M. Switching a polar metal via strain gradients. *Phys. Rev. Lett.* **126**, 127601 (2021).
48. Nova, T. F. et al. Metastable ferroelectricity in optically strained $SrTiO_3$. *Science* **364**, 1075–1079 (2019).
49. Li, X. et al. Terahertz field-induced ferroelectricity in quantum paraelectric $SrTiO_3$. *Science* **364**, 1079–1082 (2019).
50. Banerjee, S., Rowland, J., Erten, O. & Randeria, M. Enhanced stability of skyrmions in two-dimensional chiral magnets with Rashba spin–orbit coupling. *Phys. Rev. X* **4**, 031045 (2014).

Methods

Synthesis and characterization of $Ca_3Co_3O_8$ thin films

Thin films were grown on LSAT $(001)_{pc}$ substrates in a custom-designed pulsed laser deposition system using a polycrystalline $Ca_2Co_2O_5$ target. In this paper, we denote the crystalline axes of thin films according to the pseudocubic (pc) notation of the LSAT substrate. The growth temperature and oxygen pressure for $Ca_2Co_2O_5$ were optimized to be 610 °C and 6.0 Pa, respectively. The energy density of the excimer laser (λ = 248 nm) was controlled at 1.2 J cm^{-2} on the target surface, with a repetition rate of 4 Hz. After growth, the samples were cooled down to room temperature at a cooling rate of 10 °C min^{-1} under the growth pressure. The $Ca_3Co_3O_8$ samples were obtained by annealing the $Ca_2Co_2O_5$ samples at 300 °C for 3 h, within a chamber (~2 litres) filled with 1 bar of mixed ozone (5 g m^{-3}) and oxygen with a flow rate of 1 litre min^{-1}. The sample was subsequently cooled down to room temperature with the heater turned off. The crystalline structures of both $Ca_2Co_2O_5$ and $Ca_3Co_3O_8$ thin films were characterized by a high-resolution four-circle X-ray diffractometer (SmartLab, Rigaku) with a Cu $K_{\alpha 1}$ (λ = 0.15406 nm) radiation. The sample thickness was controlled with the calibrated growth rate and then further confirmed by X-ray reflectometry measurements. Most of the samples studied have a thickness between 35 and 40 nm, while slightly thicker samples were used for STEM (~56 nm), reciprocal space mapping (~83 nm) and SHG (~120 nm) measurements, to demonstrate sample uniformity, maximize the diffraction intensity and minimize the interface and surface contribution, respectively.

STEM imaging

Cross-sectional samples for STEM experiments were prepared by using a focused ion beam instrument. The high-angle annular dark field and annular bright field images were acquired on a probe-corrected STEM (FEI Titan Cubed Themis 60-300) operated at 300 kV. The convergence semi-angle was 25 mrad. The collection angle ranges of the high-angle annular dark field and annular bright field detector are ~64–200 mrad and ~8–58 mrad, respectively. Image simulations were performed using the xHREM simulation software[51].

Electron ptychography characterization

Datasets for ptychographic reconstruction were acquired using an electron microscope pixel array detector (EMPAD) equipped on the same microscope mentioned above. The convergence semi-angle was 25 mrad, and the maximum collection angle was 67 mrad. The electron probe was under-focused by about 15 nm, and the scan step size was 0.4 Å. Ptychography is a real-space phase-retrieval method using scanning coherent diffraction data[52]. To recover the object phase encoded in the so-called 4D (2D scanning in real space and 2D diffraction in reciprocal space) data, various algorithms have been proposed, in particular the probe recovery to separate the probe from the object, the mixed-state method to account for partial coherence, and the multislice method to consider multiple scattering in thick samples and to obtain depth resolution[52,53]. Recently, the adaptive propagator method was developed to correct the misorientation between probe direction and zone axis of crystals[54]. In this work, ptychographic reconstruction was conducted using adaptive-propagator ptychography, which is of critical importance for the current material since it is electron beam sensitive, making it extremely challenging to finely tune the orientation of crystals for high-precision measurements of atomic positions. During reconstruction, the sample was divided into 25 slices and the slice thickness was about 1.5 nm. Pixel size in the phase images was 0.14 Å. Six probe modes were included in the reconstruction, and the recovered probe modes are shown in Extended Data Fig. 5a. Scan positions (Extended Data Fig. 5b) were also refined to correct the relative drift between the probe and the object during data collection. For quantitative structural analysis after reconstruction, surface slices were excluded to avoid the surface contamination and damage formed during sample preparation. The remaining slices were averaged to enhance the signal-to-noise ratio. Atomic columns were fitted with 2D Gaussian peaks to obtain their positions. The relative off-centre displacement of a cobalt cation is defined with respect to the midpoint of two nearest equatorial oxygen anions.

XAS and XMCD measurements

XAS measurements at cobalt *L*-edges and oxygen *K*-edges were performed at Beamlines 4.0.2 and 6.3.1 of Advanced Light Source, Beamline 4B9B of the Beijing Synchrotron Radiation Facility and Beamline 08U1A of the Shanghai Synchrotron Radiation Facility. The XAS spectra were obtained through the total electron yield mode, with signals normalized to the photon flux measured by the photocurrent of a clean gold mesh. We carried out XMCD studies at Beamline 4.0.2 of the Advanced Light Source, with an incident angle of 30° from the surface, and 90% circularly polarized X-rays were used to gain high beam intensity. The XAS spectra were taken at room temperature, while the XMCD spectra were taken at 78 K with a magnetic field of 4 T applied along the beam incident direction. The high-field XMCD measurements were performed at Beamline 25SU of SPring-8, with a normal incident and 96% circularly polarized X-rays[55,56]. The data were taken at a series of photon energies at both right- and left-circularly polarized lights, each with a pulsed magnetic field (along the beam incident) ramping from 30 T to 0 T. The XMCD and XAS spectra were then obtained by taking the difference and average of data at opposite X-ray polarities. The measurements were carried out at 100 K. The spin and orbital moments were calculated based on the XMCD sum rule[57], which reveals a large ratio (~1/3) between orbital and spin moments.

Magnetic property and electrical transport measurements

Magnetic hysteresis loops and temperature-dependent magnetizations were measured using a magnetic property measurement system (Quantum Design) with a maximum magnetic field of 7 T. The magnetic fields were applied along both the OOP (along polyhedral stacking of $[001]_{pc}$) and IP ($[100]_{pc}$) directions. Electrical transport measurements, including the temperature-dependent resistivity and MR, were performed in a physical property measurement system (Quantum Design) equipped with lock-in amplifiers (model LI 5640; NF), in which the maximum magnetic field is 9 T. For all transport measurements, standard Hall bar configuration was adopted and the electric current was set along the $[100]_{pc}$ direction of the samples. For the OOP- and IP-MR measurements, the magnetic fields were applied along the $[001]_{pc}$ and $[010]_{pc}$ directions, respectively. High-field electrical transport measurements (including the MR and Hall effect) were performed with a steady field up to 33 T in the High Magnetic Field Laboratory, Chinese Academy of Sciences, Hefei. The MR and Hall voltages were measured simultaneously by using lock-in amplifiers (SR830) with an a.c. generated by a Keithley 6221 current source.

SHG measurements

The SHG measurements were carried out with the setup schematically shown in Fig. 3b. The fundamental light was supplied by a Ti:sapphire oscillator with a 1 kHz repetition rate and 100 fs bandwidth. The generated second harmonic light (~400 nm) from samples was filtered by colour filters and a monochromator and then detected by a photomultiplier tube. The measurements were carried out in a cryostat at the temperature range of 10 to 300 K. During the measurements, the polarization of both incident- and scattered-light beams was manipulated individually by polarizers. The incident angle, defined by the sample normal and the incident light beam, was fixed at 45°, and the polar plot was determined by rotating the polarization angle φ. $Ca_3Co_3O_8$ thin films with a thickness of 120 nm were used for the measurements to minimize the SHG contribution from the sample surface and interface, while thinner samples (~40 nm) show a consistent polar state with a clear SHG response. SHG measurements were also performed

on the LAST $(001)_{pc}$ substrate. Its negligible signal (Fig. 3a) further confirmed that the observed SHG response is due to the polar state of the $Ca_3Co_3O_8$ thin films.

DFT calculations

First-principles DFT calculations were performed using the Perdew–Burke–Ernzerhof exchange–correlation functional revised for solids (PBE)[58] with an effective Hubbard parameter[59] ($U - J = U_{eff} = 1.5$ eV) for the correlated Co orbitals as implemented in the Vienna Ab initio Simulation Package[60]. The effective Hubbard parameter was chosen in such a way as to provide the best agreement with the experimental structural data. We used a 550 eV energy cut-off for the plane waves and the projector augmented wave approach[61] to treat the core and valence electrons with the following electronic configurations: $2s^2\,2p^4$ (O), $4s^2\,3d^7$ (Co) and $3s^2\,3p^6 4s^2$ (Ca). The Brillouin zone was sampled with an $8 \times 4 \times 4$ Γ-centred **k**-point mesh. For structure optimization, we performed full relaxation of the volume, shape and atomic positions (converged to less than 0.1 meV Å^{-1}). The group-theoretical analysis was aided using the AMPLIMODES[62,63] and ISODISTORT[64] tools. We computed the phonons using the frozen-phonon approach with finite displacements of 0.01 Å and a $1 \times 1 \times 1$ supercell. Phonon frequencies were calculated from the force constants using the PHONOPY[65] code. Experimentally, the polar state exists well above the magnetic Curie temperature indicating that magnetism should not be responsible for breaking inversion symmetry. Therefore, the phonon calculations were performed imposing a collinear FM (FM1) spin configuration.

Non-reciprocal transport

For the non-reciprocal transport, an a.c. excitation with a frequency of 37.33 Hz was supplied by a Keithley 6221 current source, and we then probed both the first and second harmonic compounds of the voltage output through the lock-in amplifiers. Due to a phase shift of the non-reciprocal response, the in-phase components were recorded for R^{ω}, while the out-of-phase components were recorded for $R^{2\omega}$. To remove background signals arising from the nonuniformity of the samples, the symmetry component was subtracted as $R^{2\omega}(B) = (R_{raw}{}^{2\omega}(B) - R_{raw}{}^{2\omega}(-B))/2$. We swept the magnetic field between +9 T to −9 T, and the remanent component of $R^{2\omega}$ was recorded at zero field (after magnetic field ramping from 9 T to 0 T). The patterned Hall bar has a width of $w = 10$ µm and a length of $l = 20$ µm, and the typical film thickness is about 40 nm.

MFM measurements

MFM measurements were carried out in a magnetic force microscope (Attocube system) with a 9 T superconducting magnet and a helium refrigeration system. Commercial cantilevers (NANOSENSORS, PPPEFM, spring constant ~2.8 N m^{-1}, resonant frequency ~75 kHz) were used. The MFM images were taken at a constant height mode with the scanning plane ~100 nm above the film surface. The external magnetic field was applied perpendicularly to the film surface. By using Gwyddion software, all images were binarized at the same threshold.

Data availability

The data supporting the findings of this study are available from the corresponding authors upon reasonable request. Source data are provided with this paper.

References

51. Ishizuka, K. A practical approach for STEM image simulation based on the FFT multislice method. *Ultramicroscopy* **90**, 71–83 (2002).
52. Rodenburg, J. & Maiden, A. in *Springer Handbook of Microscopy* (eds Hawkes, P. W. & Spence, J. C. H.) 819–904 (Springer, 2019).
53. Chen, Z. et al. Electron ptychography achieves atomic-resolution limits set by lattice vibrations. *Science* **372**, 826–831 (2021).
54. Sha, H., Cui, J. & Yu, R. Deep sub-angstrom resolution imaging by electron ptychography with misorientation correction. *Sci. Adv.* **8**, eabn2275 (2022).
55. Nakamura, T. et al. Soft X-ray magnetic circular dichroism of a CoFe/MnIr exchange bias film under pulsed high magnetic field. *Appl. Phys. Express* **4**, 066602 (2011).
56. Narumi, Y. et al. X-ray spectroscopies in pulsed high magnetic fields: new frontier with flying magnets and rolling capacitor banks. *Synch. Rad. N.* **25**, 12–17 (2012).
57. Chen, C. T. et al. Experimental confirmation of the X-ray magnetic circular dichroism sum-rules for iron and cobalt. *Phys. Rev. Lett.* **75**, 152–155 (1995).
58. Perdew, J. P., Burke, K. & Ernzerhof, M. Generalized gradient approximation made simple. *Phys. Rev. Lett.* **77**, 3865 (1996).
59. Dudarev, S. L., Botton, G. A., Savrasov, S. Y., Humphreys, C. J. & Sutton, A. P. Electron-energy-loss spectra and the structural stability of nickel oxide: an LSDA+U study. *Phys. Rev. B* **57**, 1505–1509 (1998).
60. Kresse, G. & Furthmüller, J. Efficiency of ab-initio total energy calculations for metals and semiconductors using a plane-wave basis set. *Comp. Mater. Sci.* **6**, 15–50 (1996).
61. Blöchl, P. E., Jepsen, O. & Andersen, O. K. Improved tetrahedron method for Brillouin-zone integrations. *Phys. Rev. B* **49**, 16223–16233 (1994).
62. Orobengoa, D., Capillas, C., Aroyo, M. I. & Perez-Mato, J. M. AMPLIMODES: symmetry-mode analysis on the Bilbao Crystallographic Server. *J. Appl. Cryst.* **42**, 820–833 (2009).
63. Perez-Mato, J. M., Orobengoa, D. & Aroyo, M. I. Mode crystallography of distorted structures. *Acta Crystallogr. Sect. A* **66**, 558–590 (2010).
64. Campbell, B. J., Stokes, H. T., Tanner, D. E. & Hatch, D. M. ISODISPLACE: an internet tool for exploring structural distortions. *J. Appl. Cryst.* **39**, 607–614 (2006).
65. Togo, A., Oba, F. & Tanaka, I. First-principles calculations of the ferroelastic transition between rutile-type and $CaCl_2$-type SiO_2 at high pressures. *Phys. Rev. B* **78**, 134106 (2008).

Acknowledgements

This study was financially supported by the Basic Science Center Project of National Natural Science Foundation of China (NFSC) under grant no. 52388201, the NFSC (52025024), the National Key R&D Program of China (2021YFE0107900, 2023YFA1406400, 2021YFA1400100 and 2021YFA1400300), the Beijing Natural Science Foundation (grant no. Z200007), the NFSC (52161135103 and U2032218), the Beijing Advanced Innovation Center for Future Chip (ICFC), the Army Research Office (ARO) under grant no. W911NF-15-1-0017 and the National Science Foundation (NSF) under grant no. DMR-2104397. N.N. was supported by JST CREST grant number JPMJCR1874 and JSPS KAKENHI grant number 18H03676. A portion of this work was performed on the Steady High Magnetic Field Facilities, High Magnetic Field Laboratory, CAS. We acknowledge the Users with Excellence Project of Hefei Science Center CAS, 2021HSC-UE007. The high-field XMCD measurement was performed under proposal no. 2019A1344 at SPring-8 BL25SU. This research used resources of the Advanced Light Source, a US DOE Office of Science User Facility under contract no. DE-AC02-05CH11231. We acknowledge the High-Performance Computing Modernization Program (HPCMP) of the DOD for providing computational resources that have contributed to the research results reported herein.

Author contributions

P.Y. conceived the project and coordinated the studies. Jianbing Z. and M.W. fabricated the samples and performed the structural and magnetic measurements. S.S. and Jianbing Z. performed all the electrical transport measurements. D.P. and J.M.R. formulated

the theoretical models, carried out the first-principles calculations and did the group theoretical analysis with L.N.W. Q.H., Y.W., Y.L. and H.P. carried out the synchrotron spectroscopy measurements. H.P. carried out the MFM measurements. H.S., W.X. and L.L. carried out high-resolution STEM and ptychography experiments and reconstructions under the supervision of R.Y. X.X. carried out the SHG measurements under the supervision of Z.S. C.X. and L.P. provided support in high magnetic field electrical transport measurements. Y.K., M.K., H.N. and Tetsuya N. provided support for the high magnetic field X-ray circular dichroism measurements. H.I., T.L., D.Y., Tianxiang N., Jiadong Z., S.Z., N.N., C.-W.N. and Y.T. provided scientific insights. Jianbing Z., S.S., D.P. and P.Y. wrote the manuscript, and all authors discussed results and commented on the manuscript.

Competing interests

The authors declare no competing financial interests.

Additional information

Extended data is available for this paper at https://doi.org/10.1038/s41563-024-01856-6.

Supplementary information The online version contains supplementary material available at https://doi.org/10.1038/s41563-024-01856-6.

Correspondence and requests for materials should be addressed to Rong Yu, James M. Rondinelli or Pu Yu.

Peer review information *Nature Materials* thanks the anonymous reviewers for their contribution to the peer review of this work.

https://doi.org/10.1038/s41563-024-01856-6

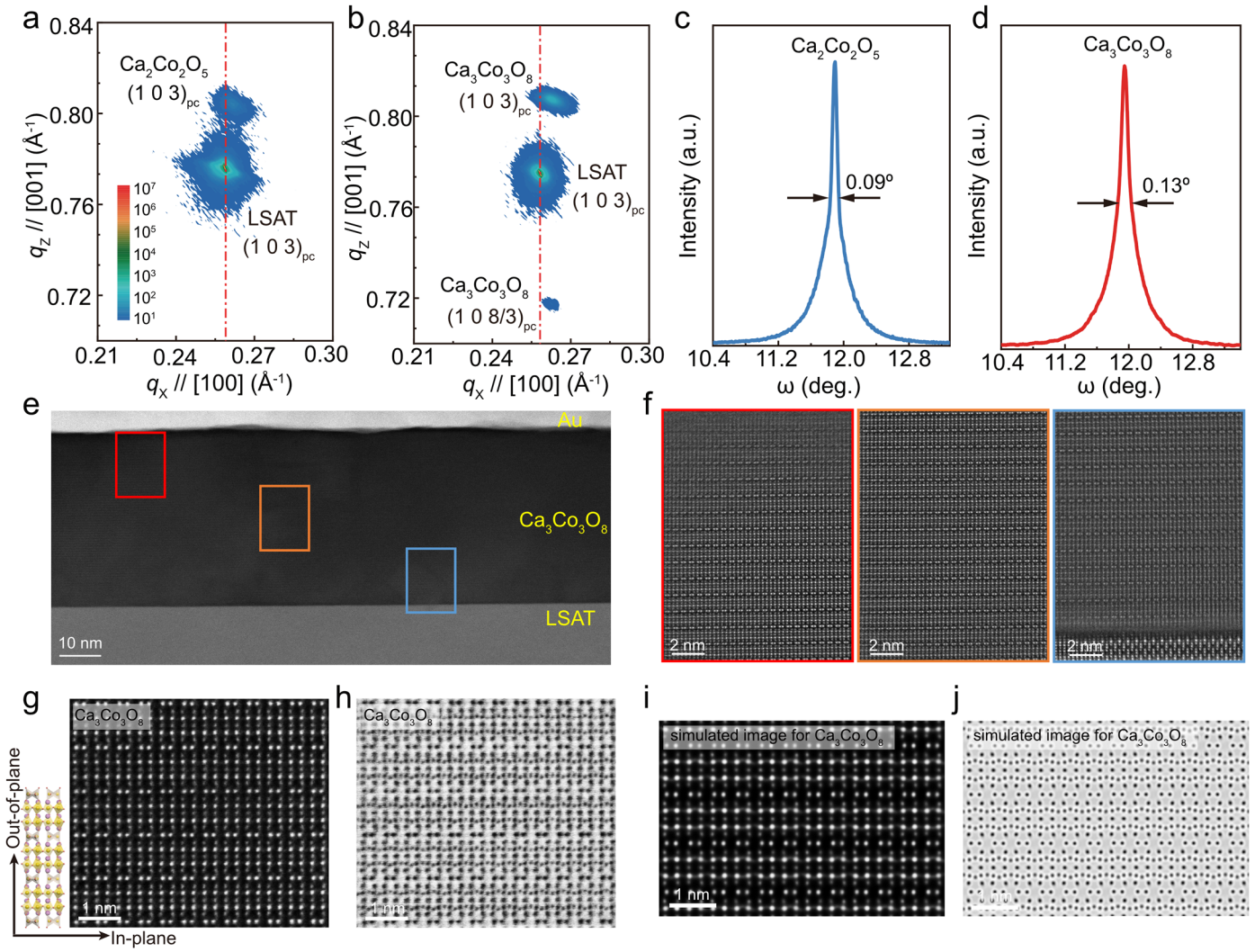

Extended Data Fig. 1 | Extended structural characterizations. a-b, Reciprocal space mappings of $Ca_2Co_2O_5$ (**a**) and $Ca_3Co_3O_8$ (**b**) thin films around the $(103)_{pc}$ crystalline plane of the LSAT substrate, in which q_x and q_z represent the projected directions in reciprocal space. The diffraction spots of both $Ca_2Co_2O_5$ and $Ca_3Co_3O_8$ were denoted based on a pseudocubic notation. **c-d**, Rocking curves around $Ca_2Co_2O_5$ $(001)_{pc}$ (**c**) and $Ca_3Co_3O_8$ $(001)_{pc}$ (**d**) diffraction peaks. **e**, STEM image of $Ca_3Co_3O_8$ thin film with a large field of view. **f**, STEM HAADF images obtained at different locations of **e**. The images in red, orange, and blue boxes correspond to regions close to the surface, in the middle region, and at the $Ca_3Co_3O_8$ film-substrate interface, respectively. A buffered layer (about one pseudocubic unit cell) can be identified at the interface, which is essential to match the different lattice constants between LSAT substrate and the newly formed $Ca_3Co_3O_8$. **g-h**, High-resolution STEM HAADF (**g**) and ABF (**h**) images of $Ca_3Co_3O_8$ thin films. The zone axis was set along the oxygen vacancy channels of $Ca_3Co_3O_8$, which is equivalent to the $[110]_{pc}$ direction of the LSAT substrate. The schematic of the atomic-scale crystalline structure is shown as reference in **g**. **i-j**, Simulated HAADF (**i**) and ABF (**j**) patterns for $Ca_3Co_3O_8$.

https://doi.org/10.1038/s41563-024-01856-6

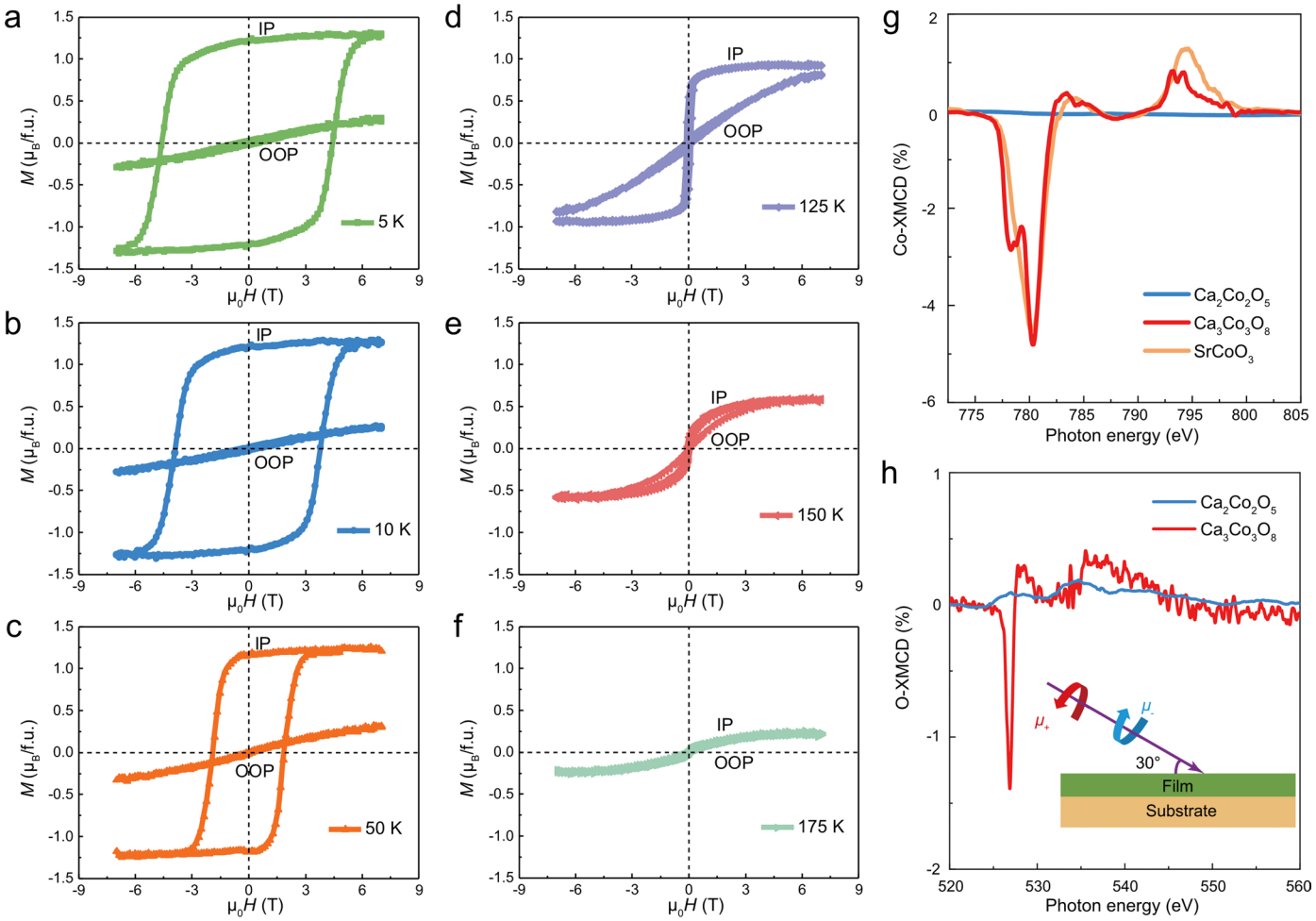

Extended Data Fig. 2 | Extended magnetic measurements of $Ca_3Co_3O_8$. **a-f**, In-plane (IP) and out-of-plane (OOP) magnetic hysteresis loops measured at 5 K, 10 K, 50 K, 125 K, 150 K, 175 K, respectively. For the IP results, the coercive field as well as the residual- and the saturated moments decrease systematically with increasing temperature. As for OOP, the coercive field and residual magnetic moment remain almost zero for all temperatures probed. **g**, Comparison of XMCD spectra at Co *L*-edges for $Ca_2Co_2O_5$, $Ca_3Co_3O_8$ and $SrCoO_3$ samples. The signal from $SrCoO_3$ is scaled by a factor of 1/3 for better comparison. **h**, XMCD spectra at oxygen *K*-edges for $Ca_2Co_2O_5$ and $Ca_3Co_3O_8$. The evident contribution to magnetization from oxygen ions indicates a strong hybridization between O 2*p* and Co 3*d* states in $Ca_3Co_3O_8$. The inset shows the experimental configuration, in which μ_+ and μ_- denote right and left circularly polarized X-rays. The spectra were taken at 78 K with a magnetic field of 4 T applied along the incident light direction. The XMCD spectral feature for $Ca_3Co_3O_8$ resembles nicely that of $SrCoO_3$, with the characteristic dip- and peak- features located around L_3- and L_2- edges, respectively. Because $SrCoO_3$ is ferromagnetic with all Co ions parallelly coupled, the suppressed XMCD in $Ca_3Co_3O_8$ suggests that only a portion of Co ions is coupled ferromagnetically. While the rest Co ions must be antiferromagnetically coupled and canceled with each other, otherwise a peak (dip) feature would be observed at the L_3 (L_2) edge. Based on the extended similarity of XMCD peak features and positions between $Ca_3Co_3O_8$ and $SrCoO_3$, we deduce that all Co ions within octahedral layers are coupled ferromagnetically, while the Co ions within tetrahedra are coupled antiferromagnetically, and furthermore the double peak features around the L_3 edge suggests a different electronic state of the Co ions within the octahedra. These are strongly supported by our first-principles calculations (Extended Data Figs. 7b, c).

https://doi.org/10.1038/s41563-024-01856-6

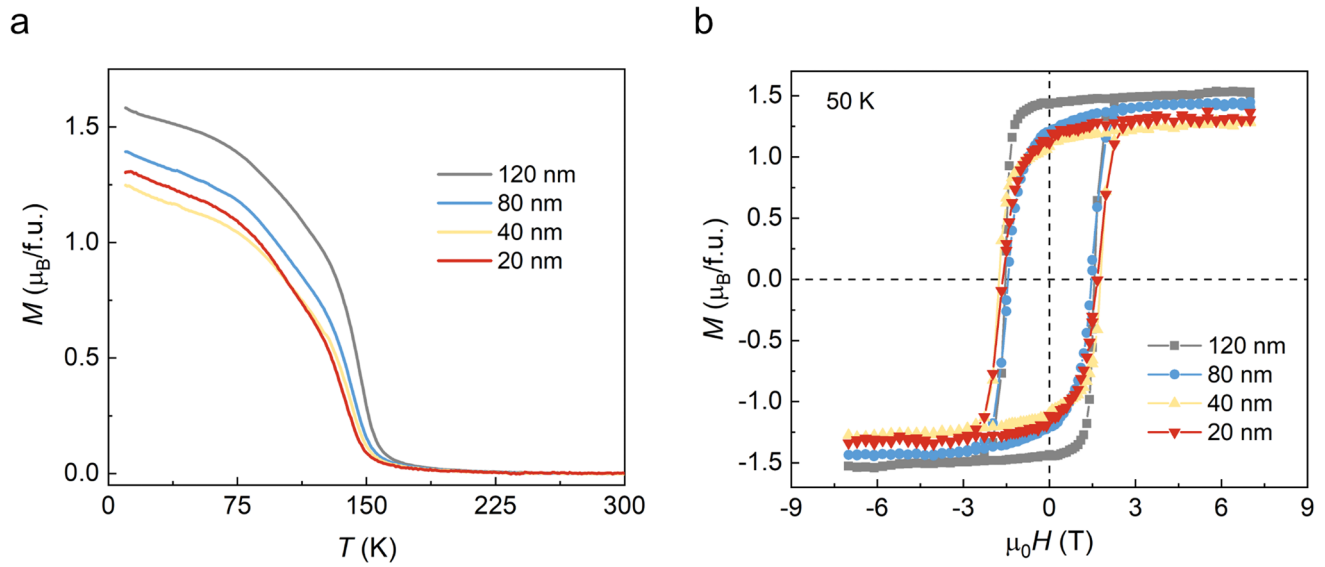

Extended Data Fig. 3 | Magnetization measurements for films with different thickness. a, Temperature dependent in-plane magnetization. The measurements were performed in a heating process at a magnetic field of 0.3 T after field cooling with a magnetic field of 7 T. **b**, Field dependence of in-plane magnetization at 50 K.

https://doi.org/10.1038/s41563-024-01856-6

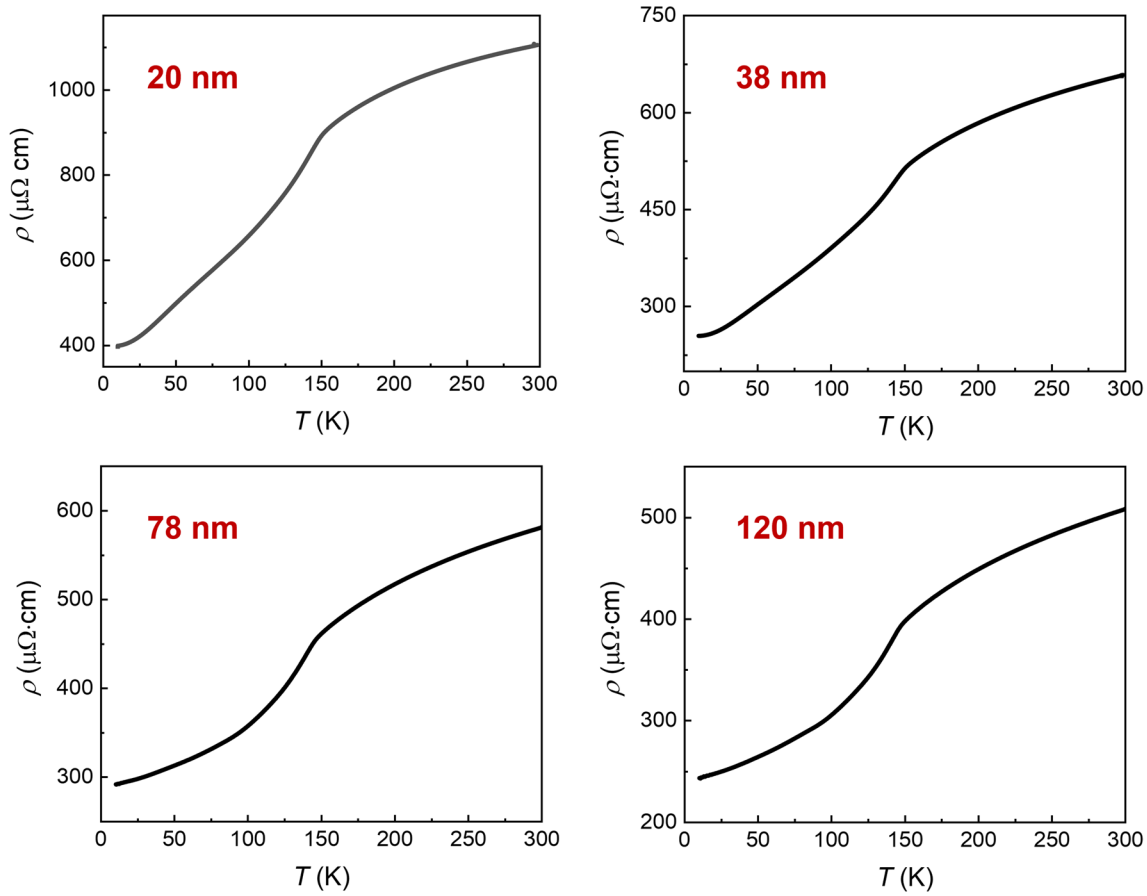

Extended Data Fig. 4 | Transport measurements for films with different thickness. All curves show similar metallic behaviors with clear kink feature at the magnetic transition temperature of ~150 K.

https://doi.org/10.1038/s41563-024-01856-6

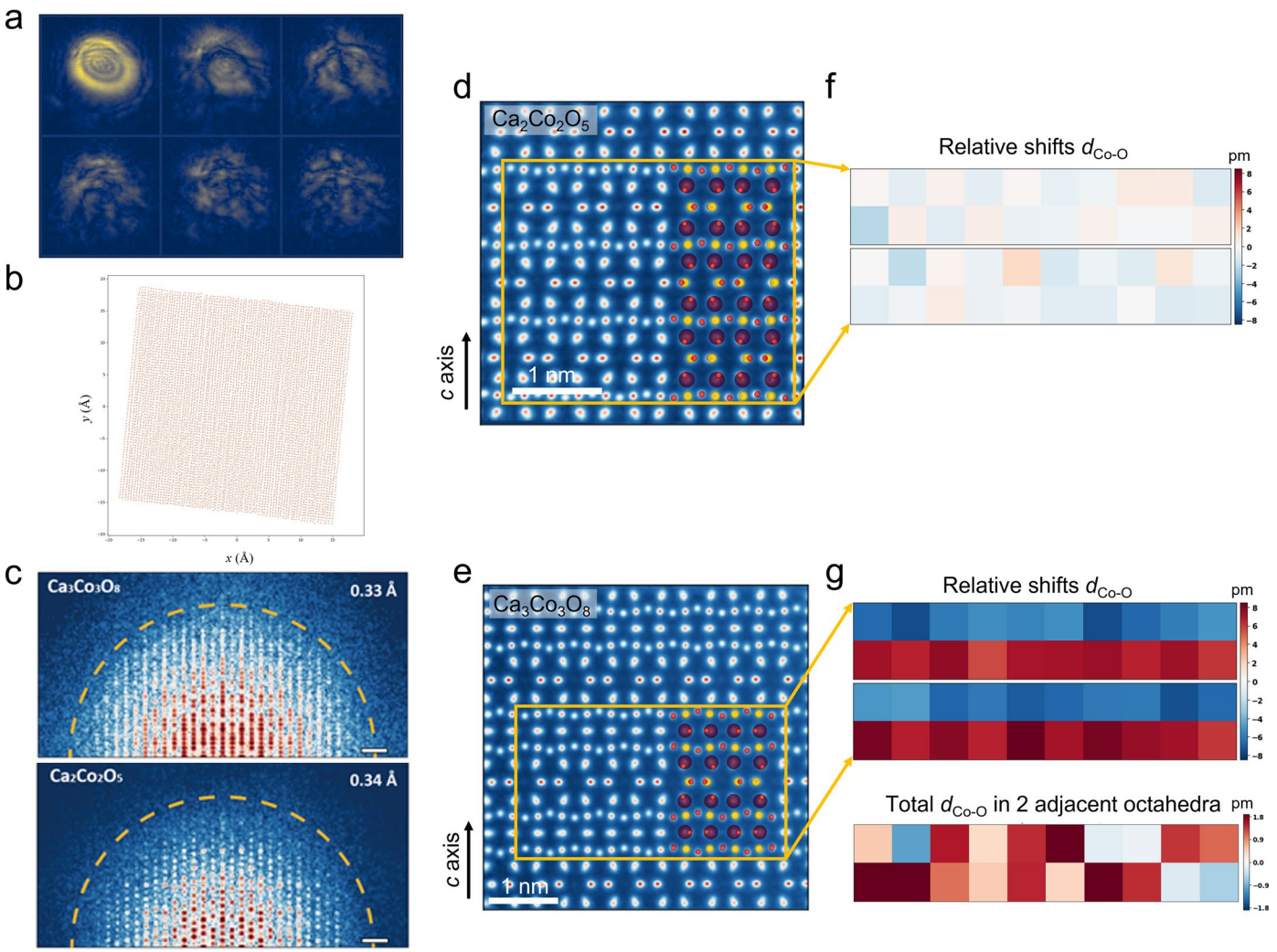

Extended Data Fig. 5 | Electron ptychography characterizations of $Ca_2Co_2O_5$ and $Ca_3Co_3O_8$ samples. a, Modulus of reconstructed orthogonal probe states at the object plane. Ratios of each state are 50.1%, 15.2%, 10.4%, 9.0%, 8.4% and 7.0%. **b**, Initial (light grey) and refined (orange) scan positions. **c**, Modulus of the Fourier transformation of the total phase images of $Ca_3Co_3O_8$ (left) and $Ca_2Co_2O_5$ (right). The information limits are 0.33 Å and 0.34 Å for $Ca_3Co_3O_8$ and $Ca_2Co_2O_5$, respectively, which are marked out with orange dotted circles. Image contrast is adjusted to show the information limit clearly. Scale bars, 0.5 nm^{-1}. **d-e**, Ptychographic phase images of $Ca_2Co_2O_5$ (**d**) and $Ca_3Co_3O_8$ (**e**). In the schematics, the yellow circles denote Co atoms, the red circles denote O atoms, and the purple circles denote Ca atoms. **f-g**, Displacements of Co atoms relative to two nearest neighbor equatorial O atoms within CoO_6 octahedral layers of $Ca_2Co_2O_5$ (**f**) and $Ca_3Co_3O_8$ (**g**). Each pixel represents a Co atomic column with its displacement ($d_{Co\text{-}O}$) along the *c* axis. In $Ca_3Co_3O_8$, there are two octahedral layers between tetrahedral layers, and the displacements in the neighboring octahedral layers are summed.

https://doi.org/10.1038/s41563-024-01856-6

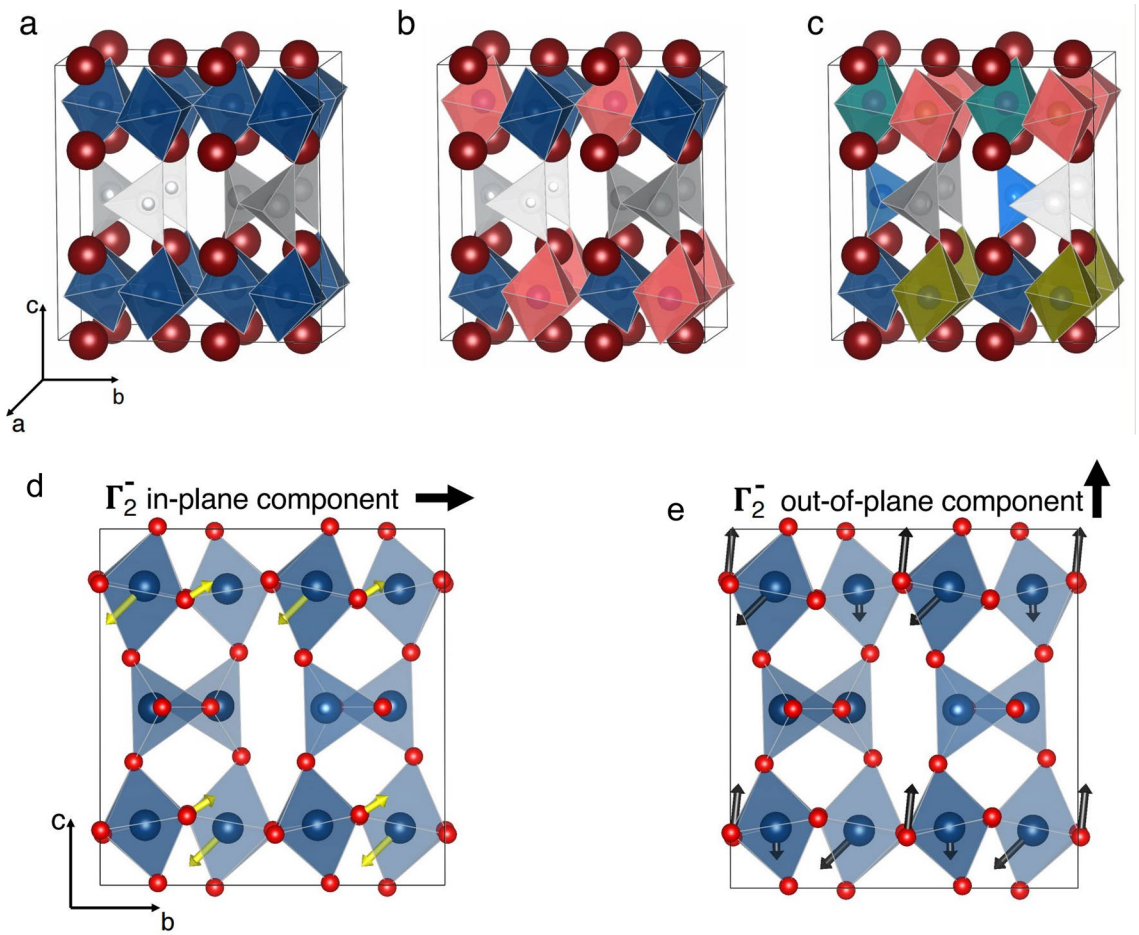

Extended Data Fig. 6 | Crystalline structure and atomic displacements of $Ca_3Co_3O_8$. a-c, Schematic crystalline structures of $Ca_3Co_3O_8$ for the centrosymmetric orthorhombic *Pbam* phase (**a**), centrosymmetric monoclinic $P2_1/c$ phase (**b**), and noncentrosymmetric monoclinic *Pc* phase (**c**), respectively. The different colors indicate the distinct Co Wyckoff sites. **d-e**, In-plane (**d**) and out-of-plane (**e**) atomic displacements of Γ_2^- polar mode.

https://doi.org/10.1038/s41563-024-01856-6

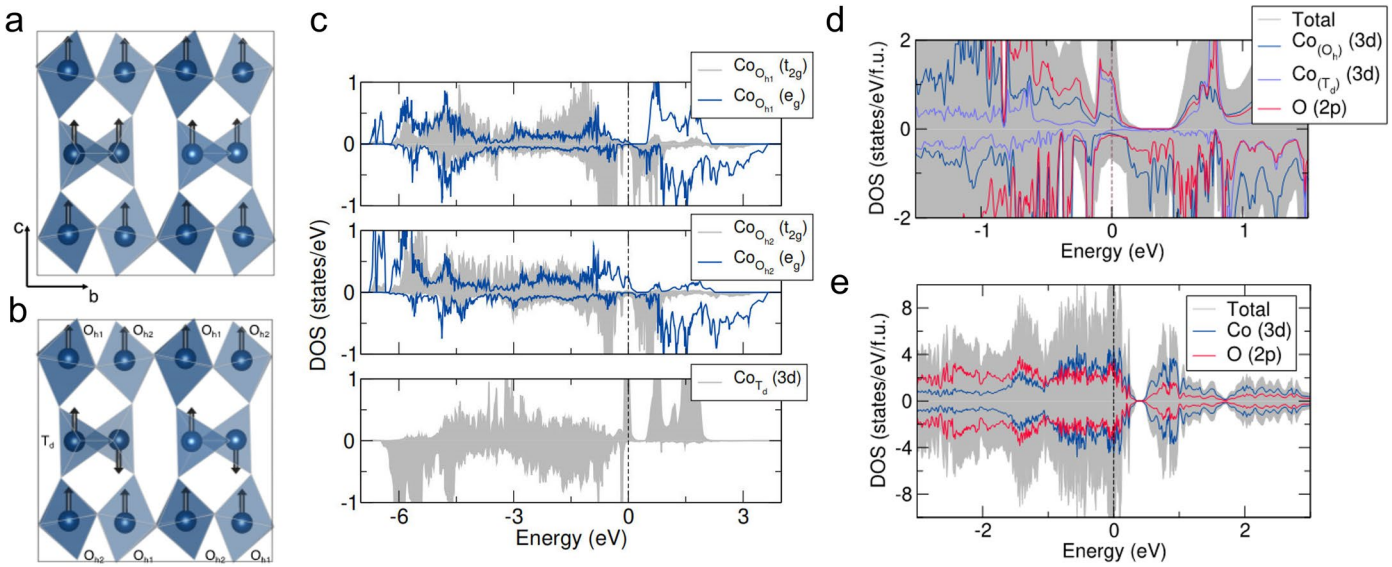

Extended Data Fig. 7 | Representative spin configurations and theoretically calculated density of states (DOS) for $Ca_3Co_3O_8$. a-b, Schematic illustrations of ferromagnetic orders among the whole lattice (FM1) (**a**) and ferromagnetic order only in the octahedral layers (FM2) (**b**). In FM2, the spins within the tetrahedral layers are coupled antiferromagnetically, and therefore have negligible contribution to the magnetization. Spin orientations on the Co sites are indicated by the solid black arrows. **c**, Site-projected DOS for $Ca_3Co_3O_8$ in FM2 *Pc* phase. The Co cations are in a $Co^{3+}\underline{L}$ state (d^6 intermediate-spin) for the O_{h1} site, and in a $Co^{2+}\underline{L}$ state (d^7 high-spin) for both the O_{h2} and T_d sites. Based on the calculations, we find an average local magnetic moment of ~2.7 μ_B for the T_d sites and an average local magnetic moment of ~1.2 and ~2.6 μ_B for the O_{h1} and O_{h2} sites, respectively. **d**, DOS for $Ca_3Co_3O_8$ in the *Pc* phase with FM2 magnetic state, which indicates the metallic nature. The atomic and angular momentum decomposed (DOS) is performed for Co atoms in octahedral (O_h) and tetrahedral (T_d) sites. **e**, DOS for $Ca_3Co_3O_8$ in the G-type antiferromagnetic *Pc* phase.

https://doi.org/10.1038/s41563-024-01856-6

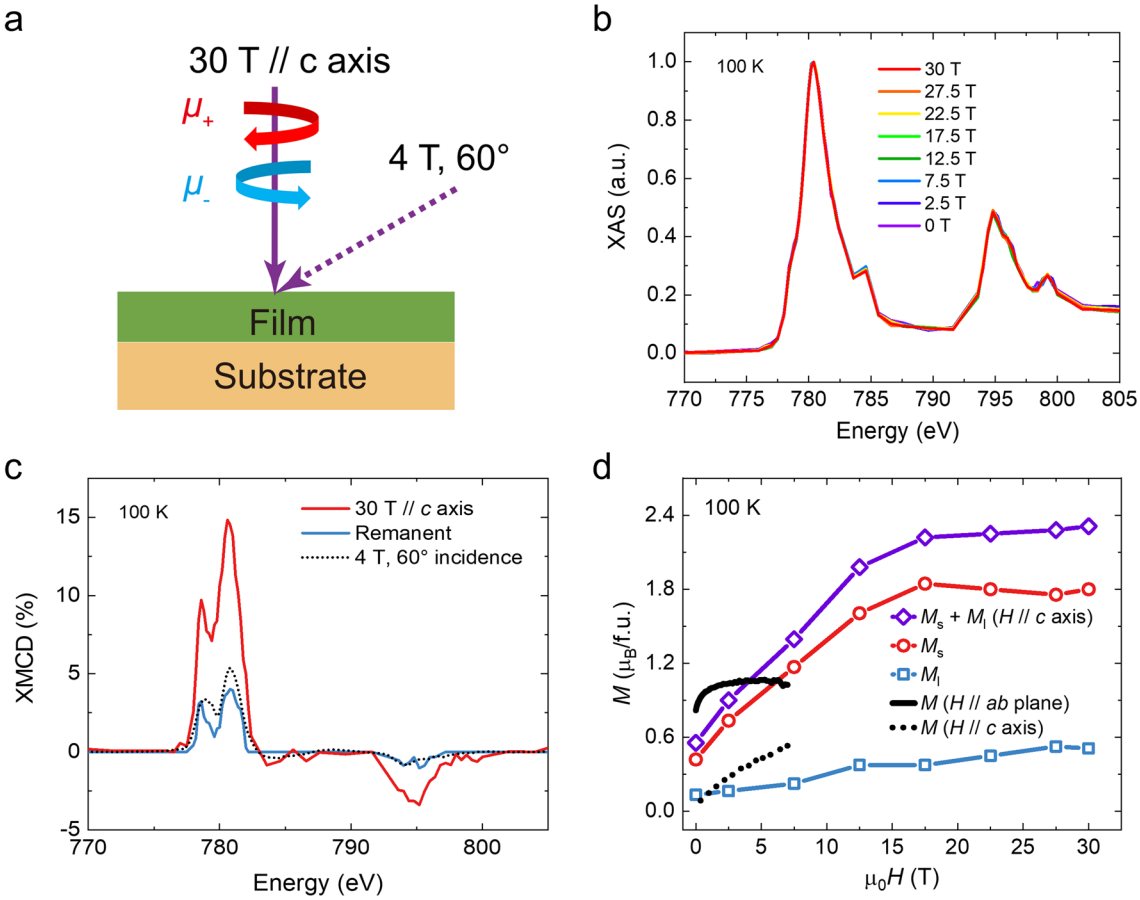

Extended Data Fig. 8 | XMCD studies of $Ca_3Co_3O_8$ at high magnetic field. **a**, Schematic illustration of XAS and XMCD measurements. **b**, Normalized XAS spectroscopy for Co *L*-edges in $Ca_3Co_3O_8$ under different magnetic fields. The identical spectra under different magnetic fields exclude the spin-state transition during the application of a high magnetic field. **c**, Comparison of XMCD spectra of Co *L*-edges in $Ca_3Co_3O_8$ at different magnetic fields. The red and blue curves with solid lines represent XMCD signals measured with the application of 30 T magnetic field along the *c*-axis, and its remnant state with zero field. The black dashed line represents the XMCD signal measured with a magnetic field of 4 T with an incident angle of 60°, which probes mainly the in-plane magnetization. **d**, Summary of field dependent magnetization in $Ca_3Co_3O_8$. The high field (up to 30 T) data (colored curves) represent the magnetic contribution of spin- (red curve), orbital- magnetic moments (blue curve) and their combination (purple curve) for Co ions, as obtained from the XMCD sum rule. Both the IP (black solid curve) and OOP (black dashed curve) magnetizations were given for the purpose of comparison. The stark differences among the high-field (purple curve) and low-field (dash line) magnetizations along the *c*-axis, as well as the saturated in-plane magnetization (black curve), demonstrate an enhanced total magnetization through a field-induced spin-flop transition. All data were measured at 100 K.

https://doi.org/10.1038/s41563-024-01856-6

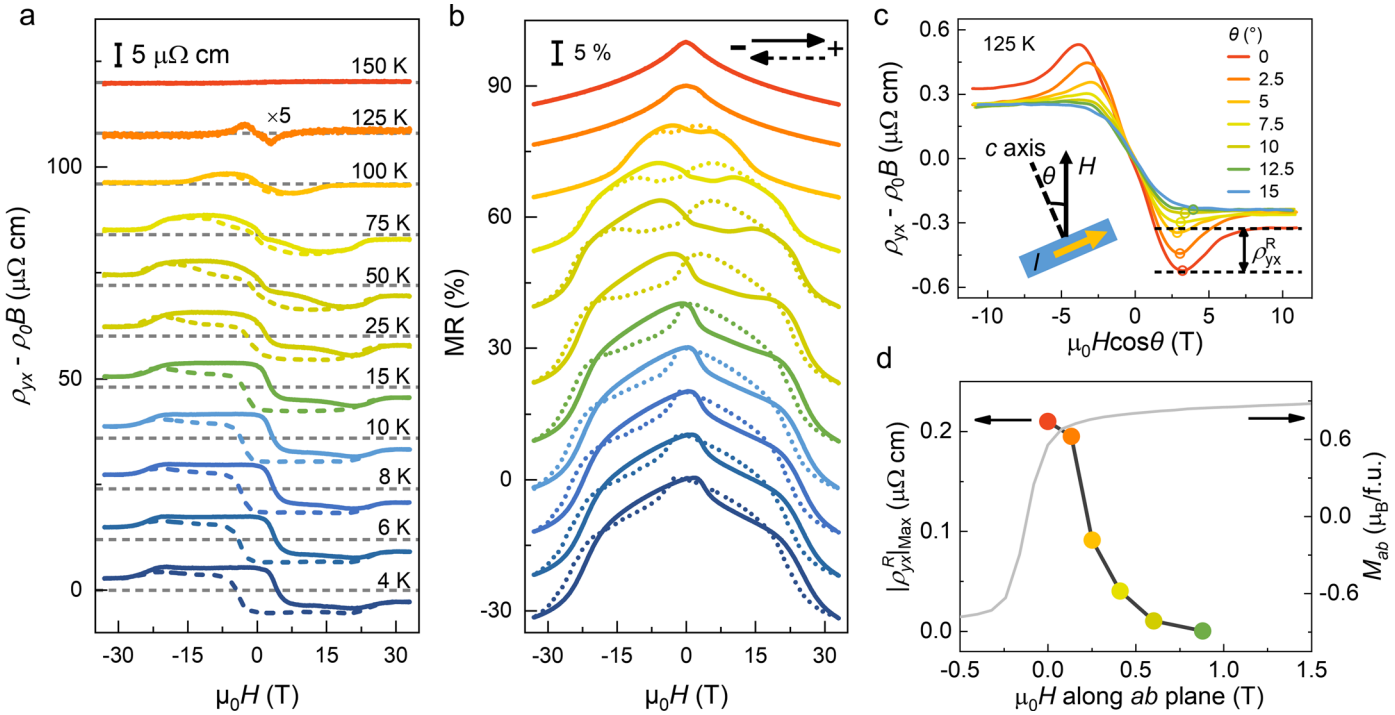

Extended Data Fig. 9 | Extended magneto-transport measurements for $Ca_3Co_3O_8$. a-b, Hall resistivity (**a**) and magnetoresistance (**b**) measured at several temperature points. The ordinary Hall contribution was removed from the Hall signal by fitting the linear background at the high field region. The Hall signal at 125 K is magnified for the purpose of clarity. **c**, Topological Hall effect (hump feature) obtained for the tilted magnetic fields. The measurements were carried out at 125 K. θ is the angle between the magnetic field and the normal (*c*) direction. The circles at the lowest Hall amplitude denote the contribution of the topological Hall signal ρ^R_{yx}. The results clearly reveal that the topological Hall signal is profoundly suppressed with the presence of an in-plane magnetic field. **d**, Evolution of topological Hall resistivity and in-plane magnetization as a function of the in-plane magnetic field, measured at 125 K. The topological Hall contribution decreases rapidly as the in-plane magnetization approaches saturation, which indicates the hump feature originates from noncollinear/noncoplanar spin configuration.

https://doi.org/10.1038/s41563-024-01856-6

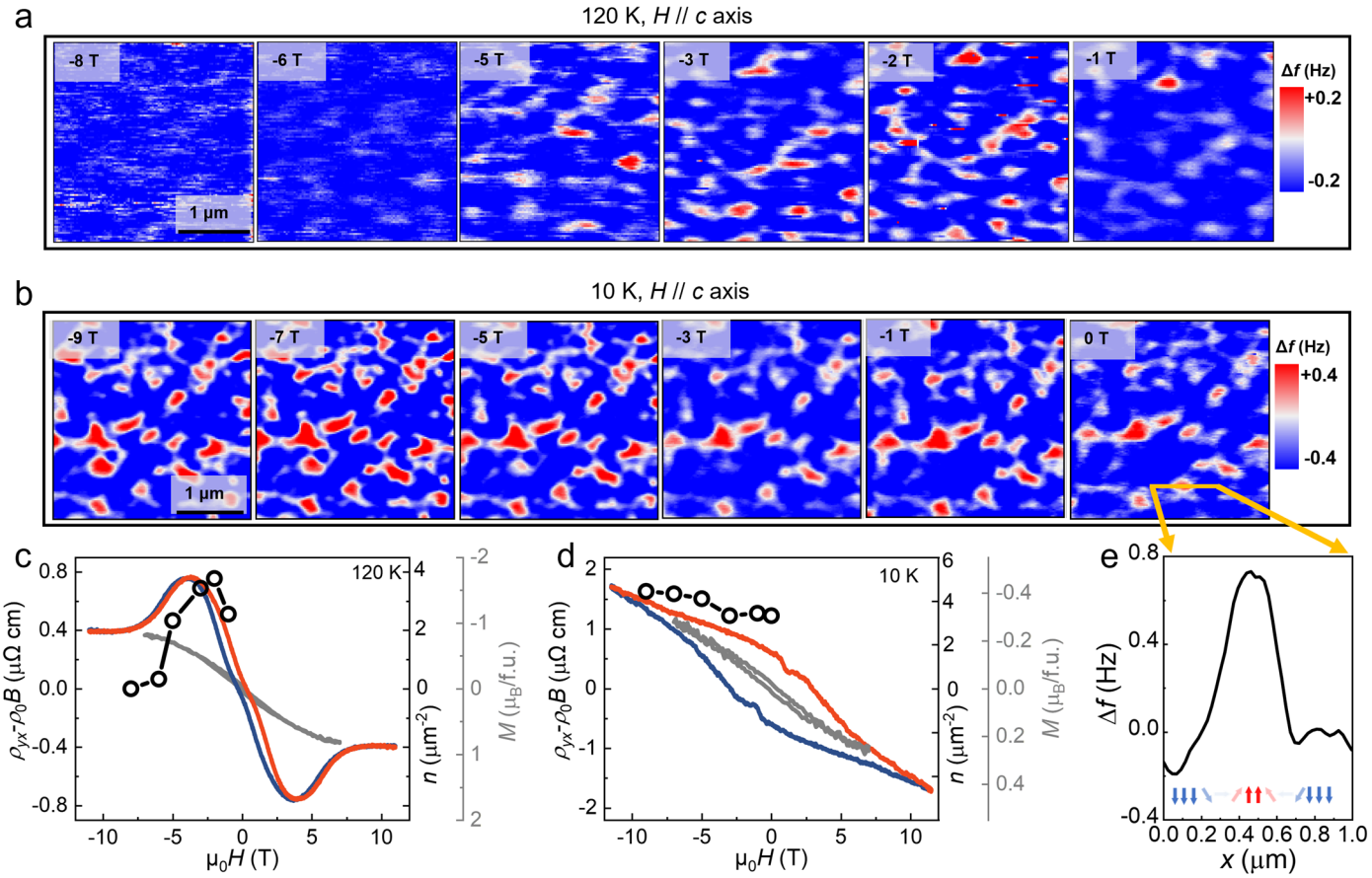

Extended Data Fig. 10 | Correlations between the topological Hall effect and the microscale magnetic domain structure. a-b, Magnetic force microscopy (MFM) images measured at (**a**) 120 K and (**b**) 10 K with different magnetic-field strengths. The magnetic field was applied along the *c* axis. **c-d**, Comparison of the topological Hall resistivity (ρ_{xy}-$\rho_0 B$, hump features of blue and red lines with increasing and decreasing magnetic field), domain density (*n*, black circles) and magnetization (*M*, gray line) as a function of the magnetic field at (**c**) 120 K and (**d**) 10 K. **e**, MFM intensity profile across an isolated domain as outlined by the yellow line in the rightmost image of (**b**). The completely suppressed MFM signal in the domain wall region indicates the formation of a Néel-type magnetic domain wall in $Ca_3Co_3O_8$. Since the $Ca_3Co_3O_8$ film shows large Dzyaloshinskii-Moriya interaction (DMI) strength (Supplementary Information Note 3) to stabilize Néel domain wall with chirality, while classical bubbles do not have any preferred chirality and are stabilized solely by dipolar interactions.